Georgia Institute of Technology

Daniel Guggenheim School of Aerospace Engineering

CCL Report 2005-009

Micro Blowing Simulations Using a Coupled Finite-Volume Lattice-Boltzmann LES Approach

S. Menon and H. Feiz

Computational Combustion Laboratory
School of Aerospace Engineering
Georgia Institute of Technology
270 Ferst Drive
Atlanta, Georgia 30332-0150
http://www.ccl.gatech.edu

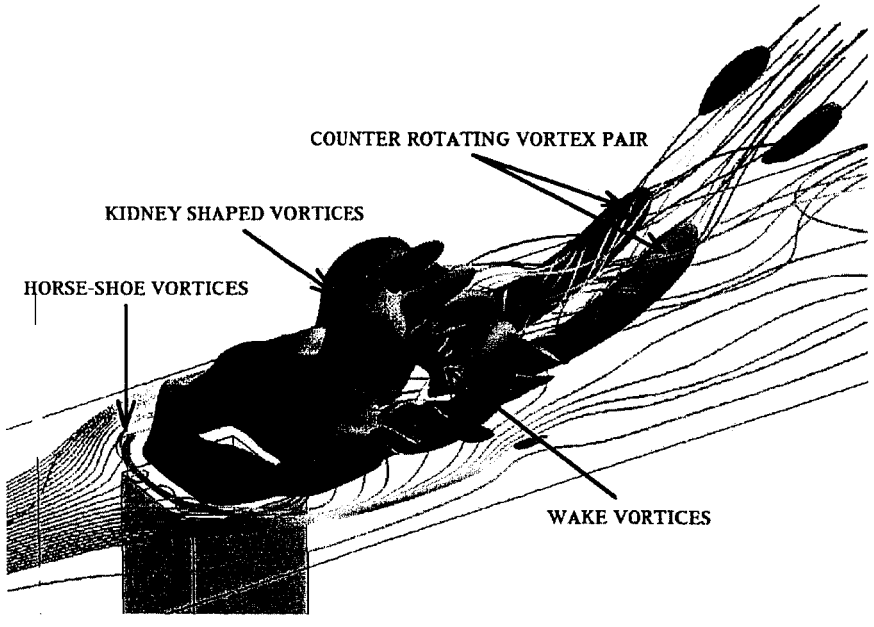

Sponsored by: *NASA Glenn Research Center*
Contract Number: *NAG3-2653*
Date: *September 2005*

TABLE OF CONTENTS

SUMMARY 1

I INTRODUCTION 1

II SIMULATION MODEL 4

2.1 FV-LES Formulation 4

2.1.1 Momentum transport closure 5

2.1.2 Energy and scalar transport closure 6

2.2 LBE-LES using Single Relaxation Time 7

2.3 LBE-LES using Multiple Time Relaxation 10

2.4 Boundary Conditions 12

2.4.1 Boundary Conditions for FV-LES 12

2.4.2 Boundary Conditions for LBE-LES 12

2.5 LBE-FV coupling 15

III NUMERICAL IMPLEMENTATION 17

3.1 Grid Stretching and Interpolation 17

3.2 Grid Resolution Issues 17

3.3 Parallel Performance of the FV-LES 17

3.4 Parallel Performance of the LBE-LES 18

3.5 Parallel Performance of the Hybrid Solver 18

IV RESULTS AND DISCUSSION 19

4.1 Jet-in-Crossflow (JICF) 19

4.1.1 Grid Resolution and Conditions 19

4.1.2 Effect of Grid and Subgrid Model 20

4.1.3 Flow features in JICF 21

4.1.4 Mean Flow 28

4.1.5 RMS and Turbulent Properties 28
4.1.6 Comparison of SRT and MRT Results 36
4.2 Hybrid FV-LBE-LES Solver Validation 36
4.2.1 Acoustic Pulse Test 39
4.2.2 Single Jet in Crossflow 41
4.2.3 Parallel Performance and scalability of the Hybrid Solver . . 42
4.3 Multiple Micro-Jets in Cross-flow 45
V CONCLUSIONS AND FUTURE PLANS 51

LIST OF FIGURES

2.1 Link vectors of f_α. 13

2.2 13

4.1 Computational domain for JICF 20

4.2 The ratio of eddy viscosity to physical viscosity 21

4.3 Instantaneous vorticity magnitude iso-surface 22

4.4 The magnitude of stream-wise velocity 23

4.5 Wake vorticities for R = 1 case 23

4.6 Instantaneous streamlines pattern 24

4.7 Sketch for structures 25

4.8 Vortex breakdown 26

4.9 Stream-wise vortices at time t = T/6 & 5T/6 27

4.10 Stream-wise vortices at time t = T/2 & 2T/3 27

4.11 Vortex shedding 27

4.12 Vortex tilting 29

4.13 Span-wise and stream-wise vorticities at time t + T/2 30

4.14 Stream-wise vorticity at time t + T/2 31

4.15 Mean stream-wise velocity profiles along the jet center and jet edge planes 32

4.16 Mean wall-normal velocity profiles along the jet center and jet edge planes 33

4.17 Comparison between LBE results (using dynamic Smagorinsky model for R=1) and experimental data (Ajersch, 1997) 34

4.18 Mean turbulence kinetic energy along the jet center plane 35

4.19 Turbulence shear stress along the jet edge plane 35

4.20 Comparison between LBE results (using dynamic Smagorinsky model for R = 1) and experimental data (Ajersch, 1997) 37

4.21 MRT results 38
4.22 Acoustic pulse 40
4.23 Acoustic pulse 40
4.24 Mass conservation plots 41
4.25 Recirculation zone 42
4.26 Mean stream-wise, spanwise and normal velocity profiles at y/D=0 . 43
4.27 Turbulent profiles at y/D=0 44
4.28 Grid configuration for multi hole simulation 46
4.29 Inflow boundary layer profile 47
4.30 Inflow boundary layer profile based on wall coordinate 48
4.31 Boundary layer profile along the jet plane 49
4.32 Velocity vectors 49
4.33 Near wall Coherent structures 50
4.34 Skin friction coefficient 50
5.1 Normal velocity at different wall normal locations 52

SUMMARY

Three dimensional large-eddy simulations (LES) of single and multiple jet-in-cross-flow (JICF) are conducted using the 19-bit Lattice Boltzmann Equation (LBE) method coupled with a conventional finite-volume (FV) scheme. In this coupled LBE-FV approach, the LBE-LES is employed to simulate the flow inside the jet nozzles while the FV-LES is used to simulate the crossflow. The key application area is the use of this technique is to study the micro blowing technique (MBT) for drag control similar to the recent experiments at NASA/GRC. It is necessary to resolve the flow inside the micro-blowing and suction holes with high resolution without being restricted by the FV time-step restriction. The coupled LBE-FV-LES approach achieves this objectives in a computationally efficient manner. A single jet in crossflow case is used for validation purpose and the results are compared with experimental data and full LBE-LES simulation. Good agreement with data is obtained. Subsequently, MBT over a flat plate with porosity of 25% is simulated using 9 jets in a compressible cross flow at a Mach number of 0.4. It is shown that MBT suppresses the near-wall vortices and reduces the skin friction by up to 50 percent. This is in good agreement with experimental data.

CHAPTER I

INTRODUCTION

In recent years, a novel drag reduction method in turbulent boundary layers has been demonstrated using a micro-blowing technique (MBT) at NASA GRC [1, 2, 3, 4, 5, 6]. Key features of this technique (in contrast to earlier more conventional blowing method) are the low effective roughness for the porous skin (achieved due to the use of micro holes) and the minimal amount of injection flow rate needed to achieve drag control. Results under laboratory and full-scale operating conditions show that significant skin friction drag reduction (as much as 50-70 percent) can be achieved using MBT. MBT appears to show even higher drag reduction in supersonic boundary layers with an added advantage of reduction of noise.

Interesting observations in subsonic flow are that the drag can be controlled by adjusting the injection flow rate and that the maximum drag reduction appears to occur within regions of adverse pressure gradient. However, more recent results in strongly adverse pressure gradient flow on a strut suggest that micro-blowing can lead to increased boundary layer and wake thickness [5] which can result in an increase in pressure drag for external flows. Thus, there are still many unresolved questions regarding the underlying physics of drag reduction as achieved by the MBT and how this blowing process impacts the large-scale flow features. Furthermore, the experimental data suggests that the injection system (and the injected airflow) couple strongly with the outer (primary) flow especially in adverse pressure gradient flow. This makes the optimization of the design of this device problematic, and parametric study using primarily an experimental approach is not a cost-effective approach.

Numerical studies of the MBT in subsonic turbulent boundary layers have also been recently reported [7] in which a steady-state 3D code was used. Only a very few micro holes and the cross-stream boundary layer were numerically modeled using a low Reynolds number turbulence closure. Results showed that for all the simulated cases, micro-blowing leads to unsteadiness due to the formation of vortices. However, due to the steady-state model employed this feature could not be studied.

MBT studies using unsteady simulation is problematic since many holes (typically hundreds) may have to be simulated simultaneously in order resolve the dynamics. Moreover, to properly capture this dynamics, the flow inside the holes has to be computed so that the flow at the hole exit plane evolves naturally (the flow can be blowing or suction depending upon the local pressure gradient). This type of requirement implies a very high computational overhead due to the increased resolution, and also due to the reduced time-step if a conventional FV scheme is employed. Clearly, an alternate technique is needed if this type of flow physics has to be simulated.

In the past, MBT studies in supersonic boundary layers were conducted [8] in which Micro-Electro-Mechanical System (MEMS) based micro-scale blowing/suction devices were simulated using direct numerical simulation (DNS) in 2D. Significant

unsteadiness is shown to be associated with the interaction between the injected fluid and the supersonic boundary layer. Vortex shedding and even pairing occur in the near field of the injected fluid in the boundary layer. By combining blowing and suction it was further shown that not only drag can be reduced but also that it can be increased at specific location.

It is clear that DNS of 3D high Reynolds number turbulent boundary layer with proper resolution of the micro holes is beyond the current and perhaps future computational capability. An alternate method that has the potential for such a study is based on large-eddy simulations (LES). In LES, all scales larger than the grid are resolved in a space and time accurate manner and only the scales smaller than the grid are modeled using a subgrid model. Although LES looks promising, it also has a serious problem in near-wall flows. To properly resolve the small-scale dynamics in the log layer, the wall normal resolution has to be close to the DNS requirement. This implies that the computational cost will be unacceptable. Clearly, an alternate method is required.

Here, we consider a hybrid approach that has the potential for dealing with the flow inside and outside the micro holes. In this approach, we combine a LBE-LES method with the conventional FV-LES method to achieve proper resolution in both regions. Both 2D and 3D LBE-LES methods have been demonstrated for fuel-air mixing and jet in crossflow in the past [9, 10, 11, 12]. In all these earlier reported studies, the flow outside and inside the injector or jet inlet are resolved completely using LBE. Thus, the flow at the jet exit plane evolves in a natural manner. The unique feature of the LBE approach is that it solves the Boltzmann equation (which, in the continuum limit recovers the Navier-Stokes equation). Since the Boltzmann equation is a single scalar equation, it is computationally very efficient (in fact, orders of magnitude faster than conventional FV algorithm). Thus, very high resolution (in fact, DNS-like resolution) can be use in the LBE model without a significant increase in the computational cost.

In the present study, the LBE model is employed primarily to resolve the flow field inside the injectors while the conventional FV-LES model is used to simulate the boundary layer flow. This approach takes the best of both worlds and couples them together within a single formulation. The LBE solver is fully coupled to the LES solver and interacts across block structured grid domains. Thus, in the injection port regions and in the near-wall region (e.g., below $y^+ = 100$), a high (DNS-like) resolution can be used, and the flow field simulated without requiring any modeling using the LBE model, while in regions away from the wall, a conventional FV LES code can be employed.

This report describes the development and the evaluation of the fully coupled LBE-LES and FV-LES simulation of turbulent jet in crossflow and multiple micro-jets in crossflow. Earlier, the single free jets and jet in crossflow (JICF) were simulated using a LBE-LES method [12, 13, 10, 14, 11] and compared to experimental data. Very good agreement was obtained. Here, we simulate the same test case using the coupled formulation and compare to earlier studies to demonstrate the applicability of this coupled method. Subsequently, the coupled solver is used to simulate a matrix of 3 x 3 micro holes in a high Mach number turbulent boundary layer. This test case

is similar to the experiment at NASA/GRC [4, 6] except that only a 3 x 3 matrix is simulated, whereas in the experiment, thousands of micro holes on a large flat plate were employed.

Here, we demonstrate this coupled approach and show the feasibility to extend this technique to handle many holes simultaneously. We also believe that these sort of sub-set simulations can be used to investigate similarity features and also to develop new scaling laws. However, due to resource and time constraints, some of the planned tasks had to be truncated. Nevertheless, as this report demonstrates, we now have a hybrid LBE-FV capability to carry out LES of this complex problem.

We have reported on our past progress elsewhere in some detail [12, 13, 10, 14]). Therefore, the details provided in these cited papers/reports are not included in this report, for brevity. Only new issues addressed subsequently are discussed in this paper. We describe the issues addressed in developing the hybrid solver and some of the validation studies. Finally, we show how this code can be used to simulate an array of micro-hole blowing into a compressible crossflow. We believe we have achieved all the key objectives of this research but full exploitation of this capability remains to be fully explored.

CHAPTER II

SIMULATION MODEL

The simulation model for the finite-volume and lattice approaches are summarized here for completeness. More details are given in the cited references.

2.1 FV-LES Formulation

Our interest here is the application of MBT to reduce skin friction drag on aircraft wings under realistic flight conditions in the Mach number range of 0.4 - 1.8. Therefore, we employ a fully compressible Navier-Stokes solver that has been used extensively in the past and is fully validated in non-reacting [15] and reacting flows [16, 17, 18]. The solver is nominally second-order accurate in both space and time; however, it also has the option for fourth order accuracy in space.

The LES equations are obtained by the application of a spatial filter to the governing equations of motion. For the compressible equations, a Favre spatial filter is employed to separate the resolved and unresolved motion [19]. For a finite-volume scheme, a low-pass, top-hat filter of the local grid size ($\overline{\Delta}$) is appropriate. The filtering operation results in the compressible LES equations.

Applying the filtering to the conservation equations results in the following LES equations:

$$\frac{\partial \bar{\rho}}{\partial t} + \frac{\partial \bar{\rho}\tilde{u}_i}{\partial x_i} = 0 \tag{2.1}$$

$$\frac{\partial \bar{\rho}\tilde{u}_i}{\partial t} + \frac{\partial}{\partial x_j}[\bar{\rho}\tilde{u}_i\tilde{u}_j + \bar{p}\delta_{ij} - \bar{\tau}_{ij} + \tau_{ij}^{sgs}] = 0 \tag{2.2}$$

$$\frac{\partial \bar{\rho}\tilde{E}}{\partial t} + \frac{\partial}{\partial x_i}[(\bar{\rho}\tilde{E} + \bar{p})\tilde{u}_i + \bar{q}_i - \tilde{u}_j\bar{\tau}_{ji} + H_i^{sgs} + \sigma_i^{sgs}] = 0 \tag{2.3}$$

In the above equations, all terms with superscript "sgs" denote subgrid quantities that require closure. Here, ρ and u_i are respectively, the mixture density and the velocity. Also, $\bar{\tau}_{ij}$ is the filtered viscous tensor (defined in terms of the filtered quantities) and $\bar{q}_i$ is the filtered heat flux vector given by

$$\bar{q}_i = -\bar{\kappa}\frac{\partial \tilde{T}}{\partial x_i} \tag{2.4}$$

In the above relations, $\bar{\mu}$ and$\bar{\kappa}$ are respectively, the filtered molecular viscosity and the thermal conductivity. These transport properties are determined as a function of the filtered quantities.

The pressure is determined from the filtered equation of state, $\bar{p} = \bar{\rho}\tilde{R}\tilde{T}$ and the filtered total energy per unit volume is $\bar{\rho}\tilde{E} = \bar{\rho}\tilde{e} + \frac{1}{2}\bar{\rho}\tilde{u}_i\tilde{u}_i + \bar{\rho}k^{sgs}$. Here, $\tilde{R}$ is gas

constant and the subgrid kinetic energy is defined as, $k^{sgs} = (1/2)[\widetilde{u_k u_k} - \tilde{u}_k \tilde{u}_k]$. Finally, $\tilde{e}$ is filtered internal energy for calorically perfect gas.

The subgrid terms that require closure are:

$$\tau_{ij}^{sgs} = \overline{\rho}\ (\widetilde{u_i u_j} - \widetilde{u}_i \widetilde{u}_j) \tag{2.5}$$

$$H_i^{sgs} = \overline{\rho}\ (\widetilde{E u_i} - \widetilde{E}\widetilde{u}_i) + (\widetilde{p u_i} - \overline{p}\widetilde{u}_i) \tag{2.6}$$

$$\sigma_i^{sgs} = \widetilde{u_j \tau_{ij}} - \widetilde{u}_j \overline{\tau}_{ij} \tag{2.7}$$

2.1.1 Momentum transport closure

The subgrid stress tensor τ_{ij}^{sgs} is closed using an subgrid eddy viscosity and a gradient diffusion model at the grid cut-off scale:

$$\tau_{ij}^{sgs} = -2\bar{\rho}\nu_t[\tilde{S}_{ij} - \frac{1}{3}\tilde{S}_{kk}\delta_{ij}] + \frac{2}{3}\bar{\rho}k^{sgs}\delta_{ij} \tag{2.8}$$

Here, the resolved rate of strain is given as $\tilde{S}_{ij} = (1/2)(\partial\tilde{u}_i/\partial x_j + \partial\tilde{u}_j/\partial x_i)$ and the subgrid eddy viscosity is ν_t. Since large-scale motion is resolved in LES, the associated counter-gradient effects at the large scales are also resolved (even though a gradient closure is employed for τ_i^{sgs} at the grid cut-off scale).

To obtain ν_t and k^{sgs}, a non-equilibrium model [20, 21] for the subgrid kinetic energy, k^{sgs} is used, and is given by :

$$\frac{\partial \overline{\rho} k^{sgs}}{\partial t} + \frac{\partial}{\partial x_i}\left(\overline{\rho}\tilde{u}_i k^{sgs}\right) = -\tau_{ij}^{sgs}\frac{\partial \tilde{u}_i}{\partial x_j} - C_\epsilon \overline{\rho}\frac{(k^{sgs})^{3/2}}{\overline{\Delta}} + \frac{\partial}{\partial x_i}\left(\overline{\rho}\frac{\nu_t}{C_t}\frac{\partial k^{sgs}}{\partial x_i}\right) \tag{2.9}$$

The subgrid eddy viscosity is modeled as: $\nu_t = C_\nu \overline{\Delta}\sqrt{k^{sgs}}$, where $\overline{\Delta} = (\Delta x \Delta y \Delta z)^{1/3}$ is based on local grid size $(\Delta x, \Delta y, \Delta z)$. There are three coefficients in the above closure coefficients, C_ν, C_ϵ, and C_t. The nominal "constant" values for these coefficients are [22, 23] 0.067, 0.916 and 1.0, respectively.

However, these coefficients can be obtained by using a localized dynamic procedure for the subgrid kinetic energy model[16, 24] (denoted as LDKM, hereafter). This dynamic procedure uses the experimental observation in high Re turbulent jet [25] that the subgrid stress τ_{ij}^{sgs} at the grid filter level $\overline{\Delta}$ and the Leonard's stress $L_{ij}(= [\langle\overline{\rho}\widetilde{u}_i\widetilde{u}_j\rangle - \frac{\langle\overline{\rho}\widetilde{u}_i\rangle\langle\overline{\rho}\widetilde{u}_j\rangle}{\langle\overline{\rho}\rangle}])$ at the test filter level $\widehat{\Delta}(= 2\overline{\Delta})$ are self-similar. Here (and henceforth), $< f >$ and $\widehat{f}$ both indicate test filtering. Since L_{ij} can be explicitly computed at the test filter level, a simple scale-similar model of the form $\tau_{ij}^{sgs} = C_L L_{ij}$, where C_L is an adjustable constant, was proposed earlier [25] but was found to lack proper dissipation.

In the LDKM model, the above observation is extended and it is assumed that L_{ij} and the subgrid stress $\widehat{\tau}_{ij}^{sgs}$ at the test filter level are also similar (i.e., $L_{ij} = \widehat{C_L}\widehat{\tau}_{ij}^{sgs}$). Using this, $\widehat{\tau}_{ij}^{sgs}$ is modelled using the same form as for τ_{ij}^{sgs} (Eqn. 2.8), except that all variables are defined at the test filter level. We define the subgrid kinetic energy at the test filter level as $k_{test} = \frac{1}{2}[\frac{\widehat{\overline{\rho}\widetilde{u_k}^2}}{\widehat{\overline{\rho}}} - \frac{\widehat{\overline{\rho}\widetilde{u_k}}^2}{\widehat{\overline{\rho}}^2}]$ and obtain a relation

$$L_{ij} = \widehat{C_L}\widehat{\tau}_{ij}^{sgs} = -2\widehat{\overline{\rho}}\widehat{C_L}C_\nu\sqrt{k_{test}}\widehat{\Delta}(\langle\tilde{S}_{ij}\rangle - \frac{1}{3}\langle\tilde{S}_{kk}\rangle\delta_{ij}) + \frac{2}{3}\widehat{C_L}\widehat{\overline{\rho}}\ k_{test}\delta_{ij} \tag{2.10}$$

In the above equation, we assume $\widehat{C_L} = 1$ and so, the only unknown is C_ν. This equation is, thus, an explicit model representation for the constant C_ν in terms of quantities resolved at the test filter level. This system of equations represents five independent equations for one unknown coefficient (and hence, is an over-determined system). The value of C_ν is determined in an approximated manner by applying the least-square method [26]. Thus,

$$C_\nu = -\frac{L'_{ij} M_{ij}}{2 M_{ij} M_{ij}} \tag{2.11}$$

In the above expression

$$L'_{ij} = L_{ij} - \frac{2}{3}\widehat{\overline{\rho}}\, k_{test}\delta_{ij} \tag{2.12}$$

$$M_{ij} = \widehat{\overline{\rho}}\, \sqrt{k_{test}}\widehat{\Delta}(\langle \tilde{S_{ij}} \rangle - \frac{1}{3}\langle \tilde{S_{kk}} \rangle \delta_{ij}) \tag{2.13}$$

A similar approach is used to obtain the dissipation coefficient C_ε such that:

$$C_\epsilon = \frac{\widehat{\Delta}(\mu + \mu_t)}{\widehat{\overline{\rho}}\, k_{test}^{3/2}} [\langle \widetilde{T_{ij}} \frac{\partial \widetilde{u_j}}{\partial x_i} \rangle - \widehat{\widetilde{T_{ij}}} \frac{\widehat{\partial \widetilde{u_j}}}{\partial x_i}] \tag{2.14}$$

where μ is the molecular viscosity and $\mu_t (= \nu_t * \overline{\rho})$ is eddy viscosity at the grid filter level. The tensor $\widetilde{T_{ij}}$ is defined as $[\frac{\partial \widetilde{u_i}}{\partial x_j} + \frac{\partial \widetilde{u_j}}{\partial x_i} - \frac{2}{3}\frac{\partial \widetilde{u_k}}{\partial x_k}\delta_{ij}]$ and $\widehat{\widetilde{T_{ij}}}$ indicates tensor at the test-filter level.

More details are given elsewhere[16, 24]. There are a few noteworthy points to highlight in this closure: (a) the LDKM approach does not employ the Germano's identity [27], (b) the self-similar approach implies that both $\overline{\Delta}$ and $\widehat{\Delta}$ must lie in the inertial range, and this provides a (albeit) rough estimate for the minimum grid resolution that can be used for a given Re, (c) the denominator in both Eqns. (2.11) and (2.14) are well-defined quantities at the test filter level, and can be directly computed, (d) the evaluation of the coefficients can be carried out locally (i.e., at all grid points) in space without encountering any instability, (e) the LDKM approach satisfies all the realizability conditions [28] in the majority of the grid points even in complex swirling reacting flows, and (f) the dynamic evaluation can be used near walls without any change [29, 30]. Finally, the computational overhead of the LDKM is not very significant since only one additional equation has to be solved.

2.1.2 Energy and scalar transport closure

In addition to τ_{ij}^{sgs}, other subgrid terms that appear in the LES filtered energy and species equations have to be closed. The subgrid total enthalpy flux, H_i^{sgs} is also modeled using the eddy viscosity and a gradient assumption as:

$$H_i^{sgs} = -\overline{\rho}\frac{\nu_t}{Pr_t}\frac{\partial \widetilde{H}}{\partial x_i} \tag{2.15}$$

Here, $\widetilde{H}$ is the filtered total enthalpy and Pr_t is a turbulent Prandtl number that can also be computed using a dynamic procedure but is currently assumed to be unity. The total enthalpy term $\widetilde{H}$ is evaluated as sum of specific enthalpy of mixture, specific kinetic energy, and specific sub-grid scale energy: $\widetilde{H} = \widetilde{h} + \frac{\tilde{u}_i \tilde{u}_i}{2} + k^{sgs}$.

The other unclosed terms such as σ_i^{sgs} are often neglected in conventional LES approaches [31] but there is no clear justification. This issue is not addressed in this study.

2.2 LBE-LES using Single Relaxation Time

The LBE method originates from a Boolean fluid model known as the lattice gas automata (LGA) which simulates viscous fluid flow by tracing the fluid motion through advection of fluid particles and particle collision on a regular lattice. LBE is an improvement over LGA in which the Boolean fluid model is replaced by a single continuous particle distribution, which is analogous to the particle distribution function in kinetic theory. This replacement eliminates the intrinsic noise inherent in LGA schemes and overcomes the shortcomings of a limited transport coefficient. The introduction of the BGK single relaxation time (SRT) model for the collision operator further simplifies the algorithm and eliminates the lack of Galilean invariance and the dependence of pressure on velocity [32, 33]. This model assumes that the particle distribution function relaxes to its equilibrium state at a constant rate, and the collision operator is similar to the classical BGK Boltzmann operator [34].

Whereas conventional Navier-Stokes schemes solve the macroscopic properties of the fluid explicitly, LBE method solves the Boltzmann equation by tracking the evolution of the microscopic particle distribution of the fluid in phase space (velocity space, physical space and time). Consequently, the conserved variables of the fluid (density and momentum) are obtained indirectly by local integration of the particle distribution (over the velocity space). The incompressible Navier-Stokes is recovered in the nearly incompressible limit of LBE using the Chapman-Enskog expansion. For the present MBT application this is an acceptable model since we are interest in using the LBE approach only within the jet injectors where the flow is at a very low speed.

Solving the lattice Boltzmann equation instead of the Navier-Stokes equation provides three distinct advantages. First, due to the kinetic nature of the LBE method, the convection operator is linear. Simple convection in conjunction with a collision process allows the recovery of the nonlinear macroscopic advection through multiscale expansions. Second, because the macroscopic properties of the flow field is not solved directly, LBE method avoids solving the Poisson equation, which proves to be numerically difficult in most finite difference methods. Third, the macroscopic properties are obtained from the microscopic particle distributions through simple arithmetic integration. More details are given in a recent review [35].

LBE method consists of two primary steps. The particles first stream to its next nearest neighbor in the direction of its prescribed velocity. Subsequently, particles of different velocities arriving at the same node interacts with each other by relaxing to its local equilibrium values which are formulated specifically to recover the low Mach

number limit of the Navier-Stokes equation. The evolution of the non-dimensional distribution function f_α is thus governed by:

$$f_\alpha(\mathbf{x}+\mathbf{e}_\alpha\delta, t+\delta) - f_\alpha(\mathbf{x},t) = \frac{1}{\tau}[f_\alpha^{eq}(\mathbf{x},t) - f_\alpha(\mathbf{x},t)],$$
$$\alpha = 0, 1, \cdots, 18 \tag{2.16}$$

where τ is the relaxation time, f_α^{eq} is the equilibrium distribution function and e_α is the particle speed in α direction. The characteristic speed is thus $c = \mathbf{e}_\alpha\delta/\delta = |\mathbf{e}_\alpha|$. Rest particles of type 0 with $e_0 = 0$ are also allowed. Note that the time step and the lattice spacing each have equal spacing of unity. Thus, $\delta = 1$. More recently, studies have demonstrated that multiple relaxation time (MRT) models can be developed when one needs to simulate scalar mixing at different Schmidt number [36]. The MRT approach has also been shown to be more stable in complex flows and in high Reynolds number flows. Therefore, we have also reviewed its performance for the present study.

In principle, there are an infinite number of possible velocity directions in the 3D velocity space. Discretizing these infinite number of velocity directions into a fixed set of velocity directions inevitably introduces discretization errors to the solution. As a general rule, the accuracy of the model to simulate Navier-Stokes flow comes at the expense of increasing computational cost resulting from the number of discrete velocities used in the model. Frisch et al. [37] have shown that the Navier-Stokes equation cannot be recovered unless sufficient discrete velocities is used to ensure lattice symmetry.

There are various 3D cubic lattice models developed, most notably the 15-bit (D315), 19-bit (D3Q19), and 27-bit (D3Q27) model [38]. Here, using common notations in scientific literatures, D is the number of dimensions and Q is the number of discrete velocities. In previous numerical simulations of a square duct, a lid-driven cavity and a circular pipe [39], no significant improvement in accuracy is observed when the D3Q27 model was used over the D3Q19 model, and thus, the D3Q19 model is assumed to be sufficiently accurate for the current purpose.

The 19-bit velocity field (Fig. 2.1) is:

$$\mathbf{e}_\alpha = \begin{cases} (0,0,0) \\ \text{for } \alpha = 0, \text{ rest particle,} \\ ((\pm1,0,0),(0,\pm1,0),(0,0,\pm1))c \\ \text{for } \alpha = 1,2,\cdots,6, \text{ class I links,} \\ ((\pm1,\pm1,0),(0,\pm1,\pm1),(\pm1,0,\pm1))\sqrt{2}c \\ \text{for } \alpha = 7,8,\cdots,18, \text{ class II links.} \end{cases} \tag{2.17}$$

Here, f_α^{eq} is given by the following form:

$$f_\alpha^{eq} = w_\alpha\rho[1 + \frac{3(\mathbf{e}_\alpha\cdot\mathbf{u})}{c^2} + \frac{9}{2}\frac{(\mathbf{e}_\alpha\cdot\mathbf{u})^2}{c^4} - \frac{3}{2}\frac{\mathbf{u}^2}{c^2}], \tag{2.18}$$

where

$$w_\alpha = \begin{cases} \frac{1}{3} & \alpha = 0 \\ \frac{1}{18} & \alpha = 1,2,\cdots,6 \\ \frac{1}{36} & \alpha = 7,8,\cdots,18. \end{cases}$$

The macroscopic properties of the flow field can be obtained by integrating the distribution functions over the velocity space:

$$\rho = \sum_{\alpha} f_{\alpha} \tag{2.19}$$

$$\rho \mathbf{u} = \sum_{\alpha} \mathbf{e}_{\alpha} f_{\alpha}, \qquad \alpha = 0, 1, ..., 18 \tag{2.20}$$

where ρ is the density and $\mathbf{u}$ is the velocity. All the macroscopic properties are obtained as function of space and time from this integration.

The Navier-Stokes mass and momentum equations are obtained by using the BGK single relaxation time model [34], and by employing Chapman-Enskog expansion are:

$$\frac{\partial \rho}{\partial t} + \frac{\partial \rho u_i}{\partial x_i} = 0 \tag{2.21}$$

$$\frac{\partial (\rho\, u_i)}{\partial t} + \frac{\partial \rho u_i u_j}{\partial x_j} = \frac{\partial (c_s^2 \rho)}{\partial x_i} + \frac{\partial 2\nu\rho S_{ij}}{\partial x_j} \tag{2.22}$$

Here, repeated indices indicate summation and $S_{ij} = \frac{1}{2}(\partial u_i/\partial x_j + \partial u_j/\partial x_i)$ is the strain-rate tensor. The non-dimensional pressure is given by the constant temperature ideal gas equation of state $p = c_s^2 \rho$ where c_s is the speed of sound with $(c_s = c/\sqrt{3})$, and $\nu = [(2\tau - 1)/6]$ is the kinematic viscosity.

For LES application we consider the filtered distribution function such that the LBE-LES form of the governing equation is

$$\bar{f}_{\alpha}(\mathbf{x} + \mathbf{e}_{\alpha}\delta, t + \delta) - \bar{f}_{\alpha}(\mathbf{x}, t) = \frac{1}{\tau_{sgs}}[\bar{f}_{\alpha}^{eq}(\mathbf{x}, t) - \bar{f}_{\alpha}(\mathbf{x}, t)]$$

$$\alpha = 0, 1, \cdots, 18 \tag{2.23}$$

where the distribution function $\bar{f}_{\alpha}$ represents only those of the resolved scales. The effect of the unresolved scale motion is modeled through an effective collision term, which in the BGK approximation is included as an effective relaxation time τ_{sgs}. The form of the subgrid correction is not fully explored at present.

In the earlier studies [12] the effective relaxation time was obtained using an eddy viscosity model (based on the Smagorinsky's eddy viscosity model) such that:

$$\nu + \nu_{\tau} = \frac{2\tau_{sgs} - 1}{6} \tag{2.24}$$

with the eddy viscosity ν_{τ} determined using:

$$\nu_{\tau} = C_{\nu} \overline{\Delta}^2 S \tag{2.25}$$

where C_{ν} is the Smagorinsky constant, $\overline{\Delta} = (\Delta_x \Delta_y \Delta_z)^{\frac{1}{3}}$ is the associated length scale and $S = |\bar{S}_{ij}\bar{S}_{ij}|$. Here, $\bar{S}_{ij} = \frac{1}{2}(\partial \bar{u}_i/\partial x_j + \partial \bar{u}_j/\partial x_i)$ is the resolved-scale rate-of-strain tensor is the characteristic filtered rate of strain tensor.

The Smagorinsky constant C_ν is determined using the localized dynamic model (LDM) [40, 24] described earlier but now adapted for the Smagorinsky's model (this is done primarily for convenience at this time). Thus, C_ν is obtained using

$$C_\nu = \frac{L'_{ij} M_{ij}}{2 M_{ij} M_{ij}} \tag{2.26}$$

where $L'_{ij} = L_{ij} - \frac{2}{3}\widehat{\bar{\rho}} k^{test} \delta_{ij}$ and $M_{ij} = -\widehat{\bar{\rho}}\sqrt{k^{test}}\widehat{\Delta}(\langle \tilde{S}_{ij} \rangle - \frac{1}{3}\langle \tilde{S}_{kk} \rangle \delta_{ij})$. Here, $L_{ij} = \widehat{\bar{\rho}}(\langle \tilde{u}_i \tilde{u}_j \rangle - \langle \tilde{u}_i \rangle \langle \tilde{u}_j \rangle)$ is the Leonard stress tensor and $k^{test} = \frac{1}{2}(\langle \tilde{u}_i \tilde{u}_j \rangle - \langle \tilde{u}_i \rangle \langle \tilde{u}_j \rangle) = \frac{1}{2} L_{kk} / \widehat{\bar{\rho}}$ is the resolved kinetic energy at the test-filter level.

This algebraic model has some inherent limitations in conventional LES and these limitations remain in effect in the LBE-LES approach. Thus, for high Re flows, the lattice resolution has to be quite high since the algebraic model requires that nearly all of the inertial range is resolved. The alternate one-equation model [24] has the ability to deal with high-Re flows on relatively coarse grid and therefore, is should be implemented for future studies.

Finally, it is worth noting that this type of closure also has some fundamental limitation in the LBE context since it is based on a model in the physical space, whereas the LBE simulation is in the phase space. A proper subgrid representation for the LBE-LES will require a closure model in the phase space to model the subgrid component of the collision integral. Such an approach still remains to be demonstrated.

2.3 LBE-LES using Multiple Time Relaxation

The simplest collision model is the linearized BGK model using single relaxation time (SRT) for all velocity bits described in the previous section. Since this model has some restrictions as well as stability issues near the sharp edges, Lallemand et. al [41] developed a generalized LBE model using multiple relaxation time (MRT). MRT model is constructed in moment space and it characterizes the instability, dissipation and dispersion of the LBE model. In addition, it provides the maximum number of adjustable parameters which can be used to optimize its properties. This section covers the formulation of the MRT.

The evolution of the non-dimensional distribution function f_α based on MRT model is governed by:

$$[f_\alpha(\mathbf{x} + \mathbf{e}_\alpha \delta_x, t + \delta_t)]_{(N+1)\times 1} - [f_\alpha(\mathbf{x}, t)]_{(N+1)\times 1} =$$

$$- [S_{\alpha\beta}]_{(N+1)\times(N+1)} \{ [f_\alpha(\mathbf{x}, t)]_{(N+1)\times 1} - [f^{eq}_\alpha(\mathbf{x}, t)]_{(N+1)\times 1} \}$$

where f^{eq}_α is the equilibrium distribution function for each velocity link of α, which goes from 0 to N. The velocity direction for each link is indicated by $\mathbf{e}_\alpha$ with the magnitude of $|\mathbf{e}_\alpha|$, which is the normalized characteristic speed of particles. As in the SRT model, the speed for rest particles is equal to zero ($e_0 = 0$) and for class I particles is equal to ratio of grid size to time step ($|\mathbf{e}_\alpha| = \delta_x / \delta_t = 1$). Note that, all time and lengths in LBE formulation are normalized by the time step and the grid

size respectively, therefore, the normalized time step (δ_t) and grid size (δ_x) themselves will be unity. $\mathbf{S}$ is the collision matrix and is designed based on its eigenvector ($\mathbf{M}$) and eigenvalue ($\hat{\mathbf{S}}$) matrices. The eigenvector matrix $\mathbf{M}$ is called moment matrix and it consists of β orthogonal basis vectors constructed by Gram-Schmidt orthogonality of the velocity links. In this study, D3Q19 link configuration is used. For this link configuration, the moment matrix is equal to:

$$M = \begin{pmatrix}
1 & 1 & 1 & 1 & 1 & 1 & 1 & 1 & 1 & 1 & 1 & 1 & 1 & 1 & 1 & 1 & 1 & 1 & 1 \\
-30 & -11 & -11 & -11 & -11 & -11 & -11 & 8 & 8 & 8 & 8 & 8 & 8 & 8 & 8 & 8 & 8 & 8 & 8 \\
12 & -4 & -4 & -4 & -4 & -4 & -4 & 1 & 1 & 1 & 1 & 1 & 1 & 1 & 1 & 1 & 1 & 1 & 1 \\
0 & 1 & -1 & 0 & 0 & 0 & 0 & 1 & -1 & 1 & -1 & 1 & -1 & 1 & -1 & 0 & 0 & 0 & 0 \\
0 & -4 & 4 & 0 & 0 & 0 & 0 & 1 & -1 & 1 & -1 & 1 & -1 & 1 & -1 & 0 & 0 & 0 & 0 \\
0 & 0 & 0 & 1 & -1 & 0 & 0 & 1 & -1 & -1 & 1 & 0 & 0 & 0 & 0 & 1 & -1 & 1 & -1 \\
0 & 0 & 0 & -4 & 4 & 0 & 0 & 1 & -1 & -1 & 1 & 0 & 0 & 0 & 0 & 1 & -1 & 1 & -1 \\
0 & 0 & 0 & 0 & 0 & 1 & -1 & 0 & 0 & 0 & 0 & 1 & -1 & -1 & 1 & 1 & -1 & -1 & 1 \\
0 & 0 & 0 & 0 & 0 & -4 & 4 & 0 & 0 & 0 & 0 & 1 & -1 & -1 & 1 & 1 & -1 & -1 & 1 \\
0 & 2 & 2 & -1 & -1 & -1 & -1 & 1 & 1 & 1 & 1 & 1 & 1 & 1 & 1 & -2 & -2 & -2 & -2 \\
0 & -4 & -4 & 2 & 2 & 2 & 2 & 1 & 1 & 1 & 1 & 1 & 1 & 1 & 1 & -2 & -2 & -2 & -2 \\
0 & 0 & 0 & 1 & 1 & -1 & -1 & 1 & 1 & 1 & 1 & -1 & -1 & -1 & -1 & 0 & 0 & 0 & 0 \\
0 & 0 & 0 & -2 & -2 & 2 & 2 & 1 & 1 & 1 & 1 & -1 & -1 & -1 & -1 & 0 & 0 & 0 & 0 \\
0 & 0 & 0 & 0 & 0 & 0 & 0 & 1 & 1 & -1 & -1 & 0 & 0 & 0 & 0 & 0 & 0 & 0 & 0 \\
0 & 0 & 0 & 0 & 0 & 0 & 0 & 0 & 0 & 0 & 0 & 0 & 0 & 0 & 0 & 1 & 1 & -1 & -1 \\
0 & 0 & 0 & 0 & 0 & 0 & 0 & 0 & 0 & 0 & 0 & 1 & 1 & -1 & -1 & 0 & 0 & 0 & 0 \\
0 & 0 & 0 & 0 & 0 & 0 & 0 & 1 & -1 & 1 & -1 & -1 & 1 & -1 & 1 & 0 & 0 & 0 & 0 \\
0 & 0 & 0 & 0 & 0 & 0 & 0 & -1 & 1 & 1 & -1 & 0 & 0 & 0 & 0 & 1 & -1 & 1 & -1 \\
0 & 0 & 0 & 0 & 0 & 0 & 0 & 0 & 0 & 0 & 0 & 1 & -1 & -1 & 1 & -1 & 1 & 1 & -1
\end{pmatrix} \tag{2.27}$$

Note that this eigenvector matrix is slightly different than what is given in Ref. [42] since the velocity links are numbered differently. Another important parameter, that can be found by this matrix, is the moments ($\mathbf{m}$) of the distribution function using $\mathbf{m} = \mathbf{Mf}$. These moments are defined as:

$$\mathbf{m} = [\rho, e, \epsilon, j_x, q_x, j_y, q_y, j_z, q_z, 3\sigma_{xx}, 3\pi_{xx}, \sigma_{ww}, \pi_{ww}, \sigma_{xy}, \sigma_{yz}, \sigma_{zx}, m_x, m_y, m_z]^T$$

where ρ, e, ϵ, j, q, σ, and m are respectively, density, kinetic energy, kinetic energy square, momentum, energy flux, traceless viscous stress tensor (with $\sigma_{ww} = \sigma_{yy} - \sigma_{zz}$), and antisymmetric third-order moment. The moments π_{xx} and π_{ww} are proportional to σ_{xx} and σ_{ww} with the factor of w_{xx} which is an additional free parameter for D3Q19 model. This parameter is equal to zero for optimized stability and is equal to -0.5 to recover the LBGK model.

The eigenvalue matrix is a diagonal matrix as following:

$$\hat{\mathbf{S}} = \text{diag}(\lambda_0, \lambda_1, \lambda_2, \cdots, \lambda_{18})$$

The diagonal elements (λ_α) of this matrix are equal to the collision frequency of the correspondent moment. Such frequencies for conserved moments (hydrodynamic variables) of density and momentum is equal to zero [42], so $\lambda_0 = \lambda_3 = \lambda_5 = \lambda_7 = 0$. The collision frequency for viscous stresses are found based on the Chapmann-Enskog analysis, which gives: $\lambda_9 = \lambda_{11} = \lambda_{13} = \lambda_{14} = \lambda_{15} = 1/\tau = 2/(6\nu + 1)$. The rest of the frequencies can be found based on linear analysis to achieve optimized stability for the model, following [42]. They are equal to:

$$\lambda_1 = 1.19, \lambda_2 = \lambda_{10} = \lambda_{12} = 1.4,$$

$$\lambda_4 = \lambda_6 = \lambda_8 = 1.2,$$

$$\lambda_{16} = \lambda_{17} = \lambda_{18} = 1.98$$

The collision term of the generalized LBE (Eqn. 2.3) can be written in terms of the moments of distribution function as,

$$[f_\alpha(\mathbf{x}+\mathbf{e}_\alpha\delta, t+\delta)]_{(N+1)\times 1} - [f_\alpha(\mathbf{x},t)]_{(N+1)\times 1} =$$

$$-[M^{-1}_{\alpha\beta}]_{(N+1)\times(N+1)}[\hat{S}_{\alpha\beta}]_{(N+1)\times(N+1)}\{[m_\alpha(\mathbf{x},t)]_{(N+1)\times 1} - [m^{eq}_\alpha(\mathbf{x},t)]_{(N+1)\times 1}\}$$

The equilibrium value of conserved moments have the same value as of their pre-collision moments, whereas non conserved moments are found as a function of the conserved moments. Scalar non-conserved moments are functions of $(\rho, |j|^2)$ and vector moments are functions of $(\rho j, j|j|^2)$. These function are given in Ref. [42].

All other issues such as the 19-velocity model and the subgrid closure issues remain unchanged.

2.4 Boundary Conditions

Many types of boundary conditions have to be implemented for both the FV-LES and the LBE-LES algorithms.

2.4.1 Boundary Conditions for FV-LES

The compressible FV-LES solver requires characteristic inflow and outflow boundary conditions [43] in order to maintain physical accuracy of incoming and outgoing pressure waves. Details are given elsewhere [43] and therefore, not repeated here. Some details related to these BCs for the hybrid solver are discussed later. On physical walls are no-slip adiabatic conditions are employed for all these simulations.

2.4.2 Boundary Conditions for LBE-LES

For the LBE solver, proper implementation of boundary conditions is very important, especially for complex geometries. On no-slip walls we employ the bounce back scheme, i.e., the particles arriving at the stationary wall is reflected back. Although easy to implement, the exact location of the no-slip wall is important. The bounce-back boundary condition exhibits second order accuracy only when the wall is place exactly halfway between the boundary node and the first fluid node [11]. Additionally, the implementation of no-slip conditions for complex wall geometries (e.g., convex and/or concave walls) are also complex. Analysis of these conditions were reported earlier but are included here for completeness.

The convention of the link vectors used in the examples is illustrated in Fig. 2.1 and their surface orientations in Fig. 2.2.

For the planar node, if a normal velocity w_{bc} is prescribed, the tangential momentums of the parallel links and the density are: $u_{tan} = (f_1 + f_7 + f_9) - (f_2 + f_8 + f_{10})$
$v_{tan} = (f_3 + f_7 + f_1 0) - (f_4 + f_8 + f_9)$
$\rho = (2(f_6 + f_{12} + f_{13} + f_{16} + f_{17} + f_0 + f_1 + f_2 + f_3 + f_4 + f_7 + f_8 + f_9 + f_{10})/(1 - w_{bc})$.
The unknown populations are therefore:

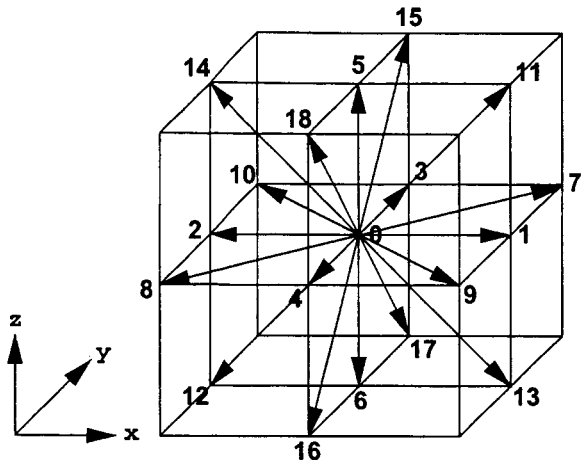

Figure 2.1: Link vectors of f_α.

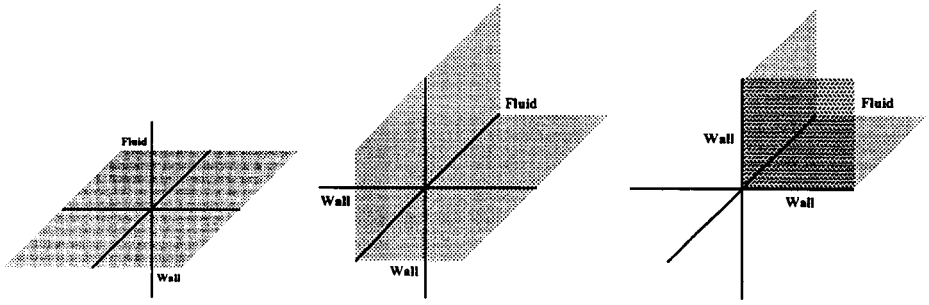

(a) Planar surface (b) Concave edge (c) Concave corner

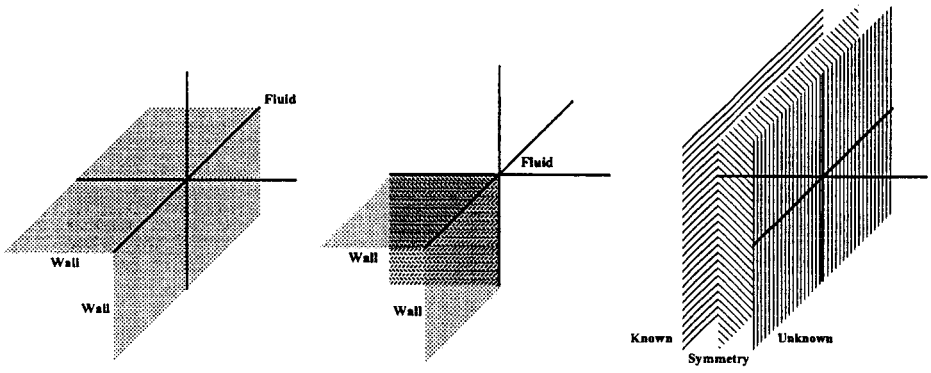

(d) Convex edge (e) Convex corner (f) Symmetric plane

Figure 2.2: Boundary geometries.

$f_5 = f_6 + \rho w_{bc}$
$f_{11} = f_{12} - 0.5u_{tan}$
$f_{14} = f_{13} + 0.5u_{tan}$
$f_{15} = f_{16} - 0.5v_{tan}$
$f_{18} = f_{17} + 0.5v_{tan}$.

For nodes on concave edge, the tangential momentum is $v_{tan} = f_3 - f_4$ and the unknowns are:
$f_1 = f_2$
$f_5 = f_6$
$f_{11} = f_{12}$
$f_7 = f_8 - 0.25v_{tan}$
$f_9 = f_{10} + 0.25v_{tan}$
$f_{15} = f_{16} - 0.25v_{tan}$
$f_{18} = f_{17} + 0.25v_{tan}$.
The *buried* links (links that do not participate in streaming but in collision) are averaged and redistributed. Thus, $f_{13} = f_{14} = 0.5(f_{13} + f_{14})$

For the concave corner, all the class I links exist in known/unknown pairs and thus: $f_1 = f_2$, $f_3 = f_4$, and $f_5 = f_6$ and
$f_7 = f_8$
$f_{11} = f_{12}$
$f_{15} = f_{16}$
$f_9 = f_{10} = 0.5(f_9 + f_{10})$
$f_{13} = f_{14} = 0.5(f_{13} + f_{14})$
$f_{17} = f_{18} = 0.5(f_{17} + f_{18})$.

Maier has pointed out that convex edges and convex corners cannot satisfy the no-slip condition with this scheme because there are insufficient unknown populations (at least one class I link) at these boundaries [44]. New treatments are devised for these boundaries and the no-slip condition is forced through the modification of the known populations as well as the unknowns. In short, the unknown populations are computed using bounce back, and the known non-parallel populations of opposite links averaged and redistributed. Subsequently, the momentum of the parallel links is redistributed to the non-parallel pairs. With this method, the total population of the known links is preserved. For the geometry in Fig. 2.2: $f_{11} = f_{12}$ and
$v_{tan} = f_3 - f_4$
$f_1 = f_2 = 0.5(f_1 + f_2)$
$f_5 = f_6 = 0.5(f_5 + f_6)$
$f_{13} = f_{14} = 0.5(f_{13} + f_{14})$
$f_7 = 0.5(f_7 + f_8) - 0.125v_{tan}$
$f_8 = 0.5(f_7 + f_8) + 0.125v_{tan}$
$f_9 = 0.5(f_9 + f_{10}) + 0.125v_{tan}$
$f_{10} = 0.5(f_9 + f_{10}) - 0.125v_{tan}$
$f_{15} = 0.5(f_{15} + f_{16}) - 0.125v_{tan}$
$f_{16} = 0.5(f_{15} + f_{16}) + 0.125v_{tan}$

$$f_{17} = 0.5(f_{17} + f_{18}) - 0.125v_{tan}$$
$$f_{18} = 0.5(f_{17} + f_{18}) + 0.125v_{tan}.$$

For the convex corner, there are no unknowns and therefore all the opposite link pairs are averaged and redistributed.

For the symmetric boundary condition, the unknown populations beyond the plane of symmetry are needed during streaming. Thus, the outgoing populations are reflected back into the domain exactly the opposite way they leave. For the geometry in Fig. 2.2, using k to denote the known outgoing populations at the i plane and uk to denote the incoming unknowns at $i+1$, the conditions are:

$$f_2^{uk,i+1} = f_1^{k,i}$$
$$f_8^{uk,i+1} = f_9^{k,i}$$
$$f_{10}^{uk,i+1} = f_7^{k,i}$$
$$f_{12}^{uk,i+1} = f_{13}^{k,i}$$
$$f_{14}^{uk,i+1} = f_{11}^{k,i}.$$

2.5 LBE-FV coupling

The two methods, LBE-LES and FV-LES have to be coupled together with full two-way interactions in order to solve the problem. Here, we achieve this coupling by combining the boundary conditions for FV and LBE models described in the previous sections. Two regions need to be properly addressed: (a) a situation when the flow is going from the FV-LES domain to the LBE-LES domain and (b) the reverse situation of flow from LBE-LES domain into FV-LES domain. In both situations inflow and outflow conditions have to be prescribed. In the present study, we are primarily interested in micro-blowing and therefore, this allows us to use some simplifications (these simplifications can be relaxed for generalize application but not addressed at present). Since the diameter of the micro hole is very small (0.5 mm) and the flow rate is also very small, we assume that the flow out of these holes is controlled by the pressure in the outer domain. Thus, when the pressure is low above the holes (relative to the pressure inside the injectors, which is determined primarily by the stagnation pressure in the injection system) then there will be outflow. On the other hand, if the pressure is higher than the exit pressure of the injector then outflow will stop and there will be no net flux. For a general purpose coupling we should allow for suction (or inflow into the injectors) to occur in the latter case. Although we have looked at this issue, we have not completed this study so far. However, for the current application this approach is considered reasonable as a first attempt to couple the two methods.

To provide characteristic "inflow" boundary conditions for the FV-LES (which is a compressible solver) one variable must be specified from inside the FV domain while four can be prescribed (and one determined by equation of state). In the present implementation, temperature at the "inflow" plane is prescribed from inside the FV domain (by simple extrapolation) while density and the three velocity components

are obtained from the LBE-LES solution from Eqs. 2.19 and 2.20. Finally, pressure is computed using the equation of state. This approach is slightly different from the approach developed for compressible inflow, as described by Poinsot and Lele [43], where velocities and temperature are prescribed and density is computed from the backward characteristic. It is possible to update temperature using an appropriate characteristic form but has not been addressed here since for all the studies so far, the temperature was nearly a constant and simple extrapolation was sufficient, as demonstrated later. We plan to revisit this issue in the near future, especially when compressibility effects have to be addressed.

To provide the "outflow" boundary conditions for the LBE-LES from one needs to prescribe all the distribution functions f_α. Some of these can be determined from the FV-LES input and some can be determined from inside the LBE-LES domain (see Fig. 2.1 for the lattice directions). In the present study, the pressure at the exit plane of the LBE domain is obtained from the FV domain (assuming zero normal pressure gradient). Then, the density is computed using $p = c_s^2 \rho$. The three velocity components at the exit plane are given from the LBE domain and then, we need to solve six equations in Eq.2.19 and Eq.2.20 along with the symmetry conditions.

The above noted coupling is spatial in nature but since temporal accuracy is needed, this coupling occurs at the proper instant in time. Here, the time scale for LBE-LES is obtained by using the characteristic scale of the injector diameter and c. This time scale is compared to the characteristic time scale for the FV-LES evolution (which is the classical CFL time-step). Both solvers evolve at their individual time steps and couple at the appropriate epoch. In the present study, the LBE-LES time step is smaller than the FV-LES and thus, the LBE field can evolve longer than the FV-LES before they need to be coupled.

CHAPTER III

NUMERICAL IMPLEMENTATION

Most of the details of the numerical implementation has been reported before and only some key comments are noted here for completeness.

3.1 Grid Stretching and Interpolation

Grid stretching can be carried out in both FV-LES and LBE-LES. For the FV-LES, the solver employs a generalized body conforming grid and so grid stretching is easy to implement. Typically, stretching less than 5 percent is used in regions of interest to maintain second order accuracy. Grid stretching in LBE-LES can also be chosen to ensure second order accuracy [11] using the interpolation supplemented Lattice Boltzmann (ISLBE). The ISLBE is implemented using the Lagrangian upwind quadratic interpolation method.

For most the reported multi-hole microblowing cases we employed a uniform grid in the LBE domain but employed a stretched grid in the FV-LES domain. At present, the grid is continuous between the two domains but there is really no need for this in this coupled approach. However, to use different grids between the two domains interpolation will have to be included. This issue will be addressed in the near future.

3.2 Grid Resolution Issues

Grid quality is very important for LES. In general, the numerical dissipation of the scheme has to be smaller than the dissipation provided by the subgrid model and this implies that both the grid and the numerical accuracy (inherent dissipation) are important. Since the current subgrid model is based on the algebraic Smagorinsky model, the overall resolution needs to be fine enough to resolve nearly all of the inertial range. Some grid resolution effects were addressed in this study using the single jet in cross-flow and are reported in the next chapter.

3.3 Parallel Performance of the FV-LES

The FV-LES is highly optimized in parallel using the message passing interface (MPI) and its performance has be well documented in many papers [45]. This solver runs on all parallel systems and maintains high scalability.

3.4 Parallel Performance of the LBE-LES

The LBE-LES solver is also implemented in parallel MPI. Optimization requires proper programming of all the boundary conditions and minimizing message passing overhead. The computational efficiency of the solver is considerable. For a single jet in cross-flow a maximum resolution of 3.25 million grid points have been used for the simulations. On Compaq SC45, the LBE-LES solver (with the localized dynamic option) costs approximately 400 single-processor hours for 5 flow-through-times and with 2.3 GB memory usage. In contrast, a conventional finite-volume solver using a similar grid would require substantially more (by 1-2 orders of magnitude) CPU hours to complete a similar simulation.

3.5 Parallel Performance of the Hybrid Solver

Both the FV-LES and LBE-LES solvers are coupled together domain decomposition to achieve proper load balancing. In order to couple the two parallel codes, different MPI groups are defined. Thus, the two codes are parallelized and implemented independently and they are coupled through a driver code using message passing. This approach allows independent control of both solvers and makes it very easy to use LBE-LES in many injector holes without requiring major code revision. Therefore, extension of this approach to many hundreds of injectors will not be a major issue (other than the computational cost).

CHAPTER IV

RESULTS AND DISCUSSION

Here, we report on some of the earlier results and new results since the last report.

4.1 Jet-in-Crossflow (JICF)

Jet in cross flow (JICF) is a canonical flow that models fuel jet injection in realistic devices. In addition, JICF occurs in other real applications, such as, vertical and short takeoff/landing (V/STOL) aircraft, internal cooling of turbine blades, dilution air jets in combustion chamber of gas turbine engines, etc. In the present context, JICF is a generic subset for the MBT approach. Many complex features are observed in JICF. In particular, three major structures have been identified in JICF:(1)the horse-shoe vortices that form ahead of the jet due to separation of the wall boundary layer [46], (2) the vortices that form along the jet shear-layer, and (3) the counter-rotating vortex pair (CRVP) that forms in the far wake aligned in the direction of the jet [47]. The interaction between these various vortical structures is very complex and still not very well understood. For example, it is generally accepted that the source of CRVP is the vortices in the jet shear layer but the exact transition from one to the other is still under investigation.

There are several parameters that impact the JICF structures and have been studied in the past. Jet to cross flow momentum ratio R and Reynolds number are the key parameters [48]. For low-speed single species flows, the velocity ratio can be used instead of the momentum ratio. Additional parameters include the effect of injection angle, such as the effect of pitched and yeawed injection [49], and the effect of the hole exit geometry [50]. As noted by Hwang [6], in the MBT case, the micro holes are drilled using laser and all these holes have irregular shapes. We limit ourselves to square holes in this study for three primary reasons: (a) the LBE approach as implemented here cannot handle curved surfaces, (b) the approximation of the irregular micro-holes using a rectangular hole is considered reasonable [6] and (c) there is a reasonable experimental data base for a single rectangular jet in cross flow [51] with which comparison can be carried out for validation.

Note that most recently, we have extended the LBE model to deal with curved surfaces but this capability has not be fully implemented here.

4.1.1 Grid Resolution and Conditions

The experiment of Ajersch *et al.* [51] is chosen as a benchmark case for validation and to investigate in some detail. The dimensions of the computational domain are shown in Fig. 4.1. The simulation is carried out at Reynolds number of 4700, based on the jet velocity and the nozzle width d. Two cases with jet-cross-flow velocity ratio of

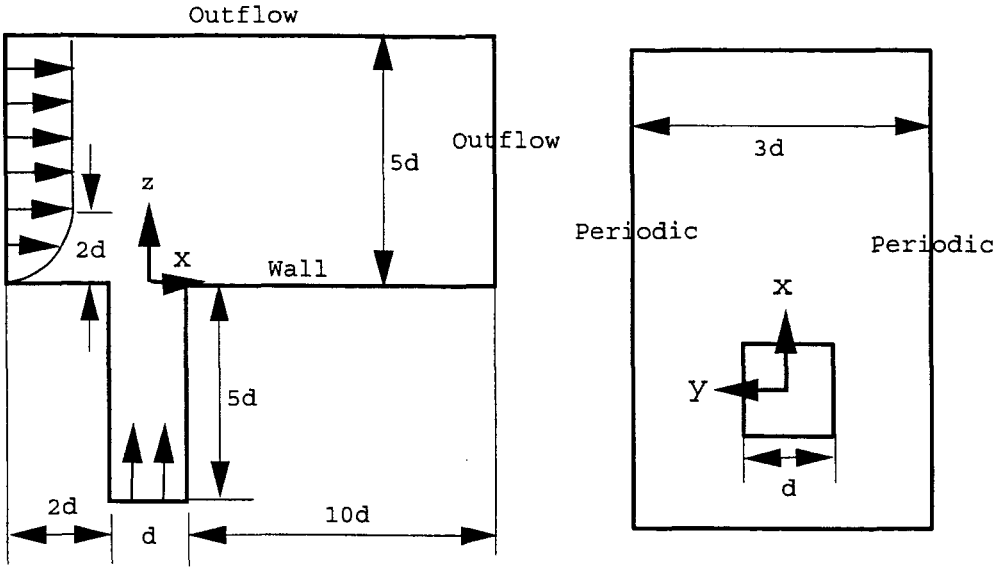

Figure 4.1: Geometry and computational domain for the jet in crossflow.

Grid	resolution	time step	$\frac{\Delta}{\eta}$	$max(\frac{\nu_T}{\nu})$
Dense	50 x 50 x 100	2.3E-06	10	8.0
Coarse	26 x 26 x 60	4.6E-06	22	3.0

Table 4.1: Coarse and dense grid distribution. Δ is the grid size and η is the Kolmogorov scale.

0.5 and 1 are simulated. The cross flow velocity profile is initialized with a boundary layer thickness of $2d$. The computational domain is resolved using $200 \times 150 \times 100$ for the crossflow domain and $50 \times 50 \times 100$ for jet section. Thus, a total of 3.25×10^6 grid points is used to discretize the entire domain. Periodic conditions are used in the span-wise direction to simulate a single square jet out of a row of six used in the experiment. On the top surface slip condition is used and at the exit outflow conditions are prescribed. The incoming jet pipe velocity profile with constant value is prescribed in the pipe a distance of 10d below the flat plate allowing the flow to develop naturally as the jet merges into the crossflow.

Results are compared with the experiment of Ajersch and numerical results obtained by Hoda *et al* [52]. Standard $k - \epsilon$ [53], a high-Re, $k - \epsilon$ model of Launder-Tselepidakis [54], and two-layer turbulence model of Chen [55] have been used in Hoda *et al* studies and therefore, offers an opportunity to compare the current LBE-LES results against these different finite-volume closure methods.

4.1.2 Effect of Grid and Subgrid Model

Results for a coarse and a dense grid for R = 1 are compared. Table 4.1 gives the relevant parameters.

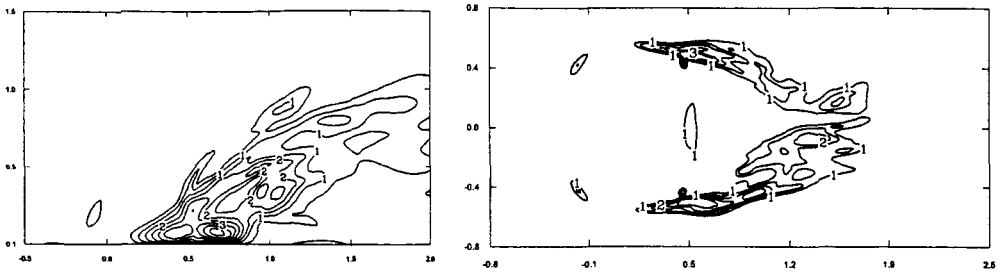

(a) Dense grid (y/d = -0.5)

(b) Dense grid (z/d = 1.5)

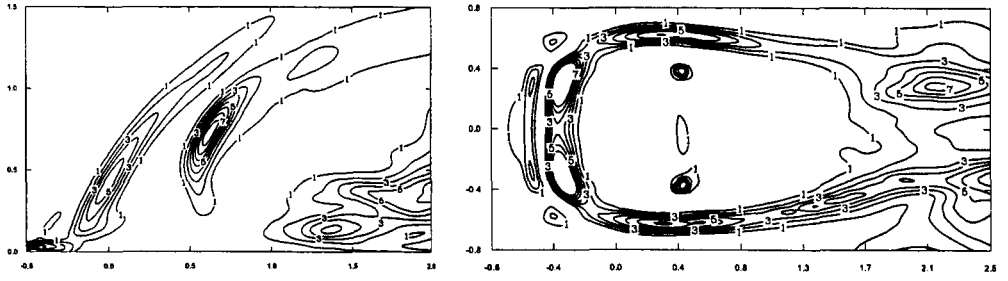

(c) Coarse grid (y/d = -0.5)

(d) Coarse grid (z/d = 1.5)

Figure 4.2: The ratio of eddy viscosity to physical viscosity at $y/d = -0.5$ and $z/d = 1.5$ for case R = 1 for (a,b) dense grid and (c,d) coarse grid.

Figures 4.2 (a)-(d) compare the ratio of eddy and physical viscosity for the coarse and dense grid cases. Parts (a) and (b) show the contours at the cross sections of $y/d = -0.5$ and $z/d = 1.5$, respectively, for the dense grid. Coarse grid viscosity ratio contours are shown in parts (c) and (d) for these same locations. The maximum viscosity ratio for the coarse grid is about 8, whereas for dense grid is about 3, which is qualitatively as expected since eddy viscosity should increase with decrease in grid resolution. Furthermore, the eddy viscosity for coarse grid is seen in more regions than dense grid, which supports the validity of the localized dynamic model for the subgrid model.

4.1.3 Flow features in JICF

It is well established in the literature [32, 50] that the jet in crossflow generates a complex flow topology due to the highly 3D and unsteady nature of this flow. All these features have been resolved in our simulation. Here, we discuss the typical features of this flow to demonstrate the accuracy of the current LBE-LES approach. Figure 4.3 shows a 3D perspective of a typical flow showing vortical features. It can be seen that the horse-shoe vortex at the leading edge of the jet is clearly seen along with its interaction with the vortices in the jet shear layer as the jet turns towards

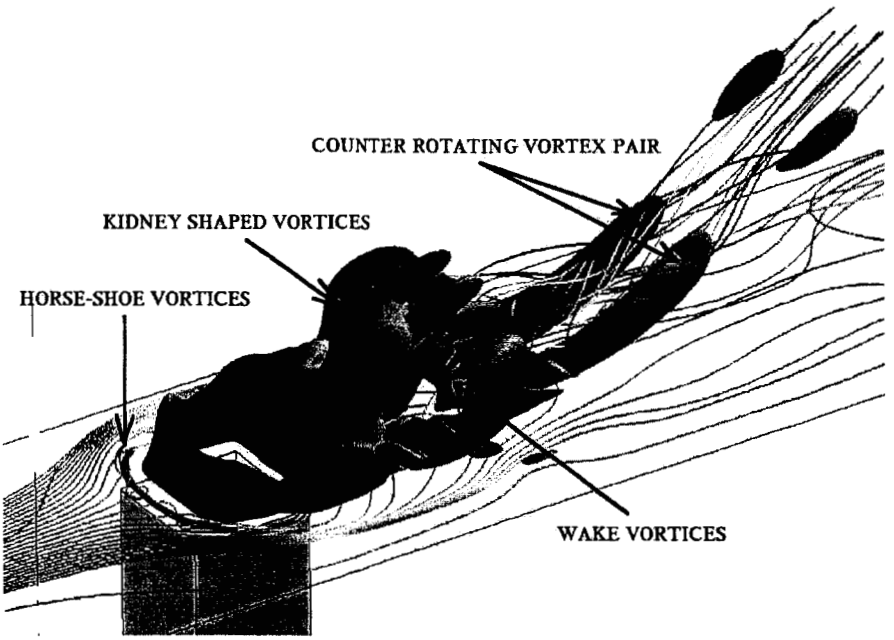

Figure 4.3: Instantaneous vorticity magnitude iso-surface $|w| = 0.003$. Horse-shoe structure (near the wall) and CRVP (following the jet trajectory) are observed (R = 1).

the outflow direction. Kidney-shaped vortices form along the shear layer, as observed earlier [32]. Further downstream, the jet is fully oriented towards the outflow and contains the classical counter rotating vortex pair (CRVP) seen in nearly all JICF experiments. The streamline pattern shown in this figure also shows how the crossflow goes around the jet and forms a recirculation region in the wake of the jet.

At the lee side of jet, the jet deflects by the cross flow and further downstream creates a recirculation region. The size of this recirculation zone is about $1.5d$ for R = 1, as measured based on stream-wise velocity at the jet center at $z/d = 0.05$, 0.1, and 0.3 and shown in Fig. 4.4. This figure also shows that there is a very small reverse flow at the leading edge with the size of $0.25d$. This region is related to the horse-show vortex that forms on the leading edge of the jet and may be the result of an adverse pressure gradient caused by the blockage effect of the jet.

The origin and formation of the vortices in the wake have been investigated earlier experimentally [46]. They examined the direction of wake vortices and horse shoe separation at the jet sides. Figure 4.5 shows the normal vorticity at $z/d = 0.2$ in the LBE simulation. The wake vorticity at the right side of the jet (shown in black) rotates in clock-wise direction and the left side vorticity has counter clockwise rotation. The rotational direction of wake vortices is consistent with the experiments [46]. The separation of flow at the lee-side of the jet is also clear in this picture. Vortex shedding downstream of crossflow is captured as well.

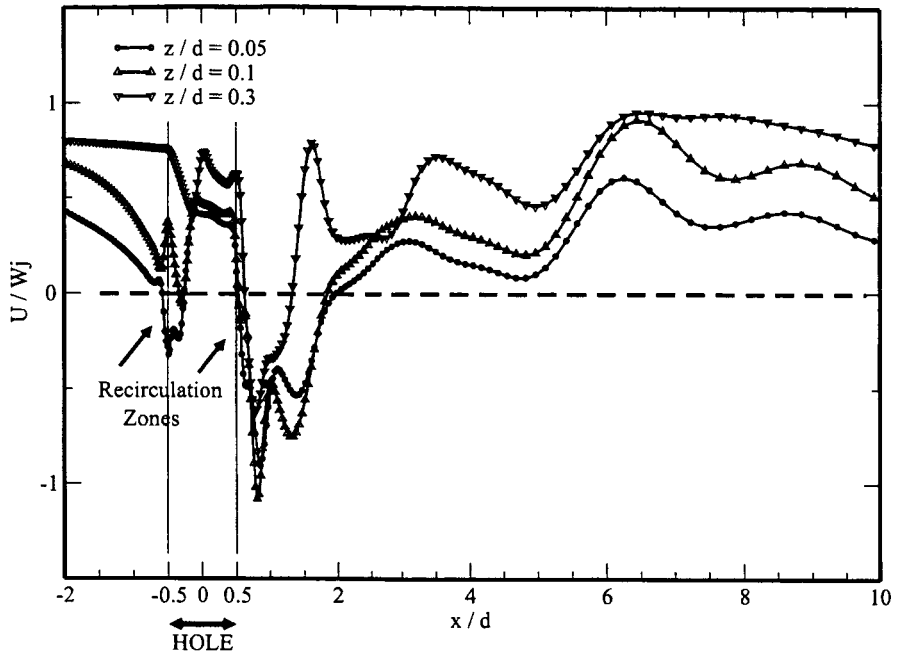

Figure 4.4: Normalized streamwise velocity along the stream-wise direction at z/d = 0.05, 0.1, 0.3 for R = 1.

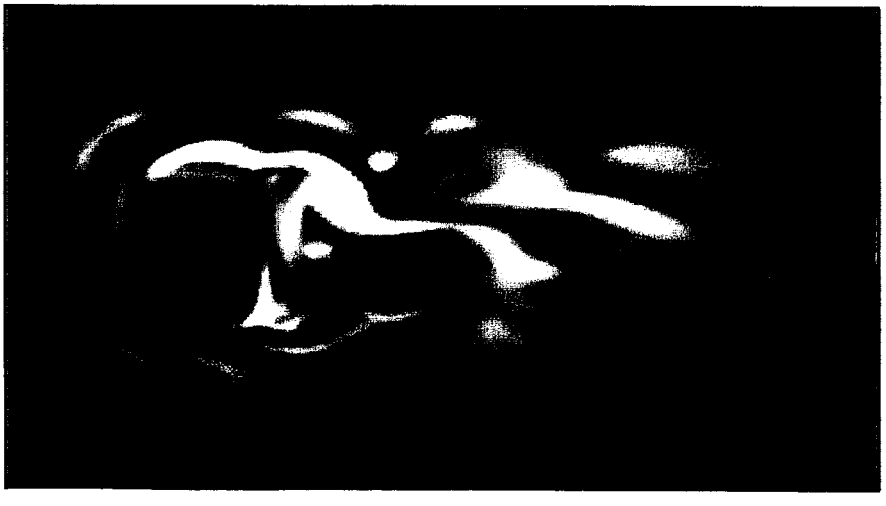

Figure 4.5: Normal vorticity magnitude at the normal cross section plane shows the footprints of vorticities at the lee side of the jet (R = 1).

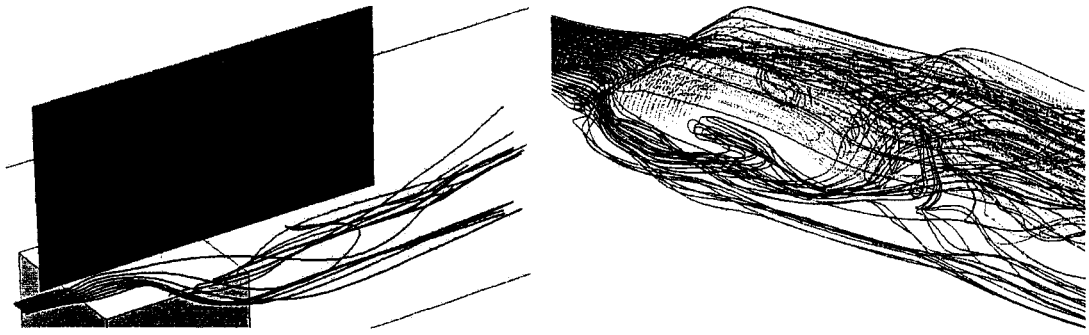

(a) Flow through hanging vortex (b) Flow in the wake of the jet

Figure 4.6: Instantaneous streamlines pattern in the side and wake of the JICF. Horse shoe streamlines at the lee side of the jet follow a spiral path in the wake of the jet (R = 0.5).

Figure 4.6 shows two sets of instantaneous streamlines. One set originates within the jet, and the second set originates from the crossflow boundary layer upstream of the jet exit. It can be seen that part of the crossflow is entrained into the wake region while some of it is lifted off into the jet shear layer region. There is substantial interaction between the jet shear layer and the crossflow boundary layer on the lee side of the jet.

The transient solution of JICF can be used to further highlight the complex flow around the CRVP. Analysis is performed for one shedding cycle of the jet with period of T = 0.002 (s). This analysis shows how vortices are stretched or realigned in different directions and illustrates the origination of CRVP.

A schematic sketch shown in Fig. 4.7 identifies the vorticity structures in the flow field. In this figure, span-wise vorticity at the lee side of the jet and kidney vortices are shown by shaded color. In addition, jet side stream-wise vorticity, vertical vorticity and CRVP are shown in gray, white and spotted color, respectively. As shown the vortex interaction is highly 3D with vorticity in one direction changing into vorticty in another direction during the interaction process.

The steam-wise vorticity is shown in Fig. 4.8 (a), where dark blue indicates the positive value (+1) and the light blue marks the negative value (-1). These structures appear at the lateral side of the jet due to the gradient of normal velocity ($\frac{\partial W}{\partial y}$) at the jet boundary layer and the gradient of span-wise velocity ($\frac{\partial V}{\partial z}$) because of the higher cross flow deflection near the wall. These structures twist and liftoff from the wall region and are torn further downstream (or will change into vorticity in another direction). In the past, the location of the vortex breakdown is determined by plotting the variation of axial velocity component through a path-line passing through a jet side stream-wise vorticity. The location of such breakdown can be recognized where there is a "drop" in the velocity component. To identify this,

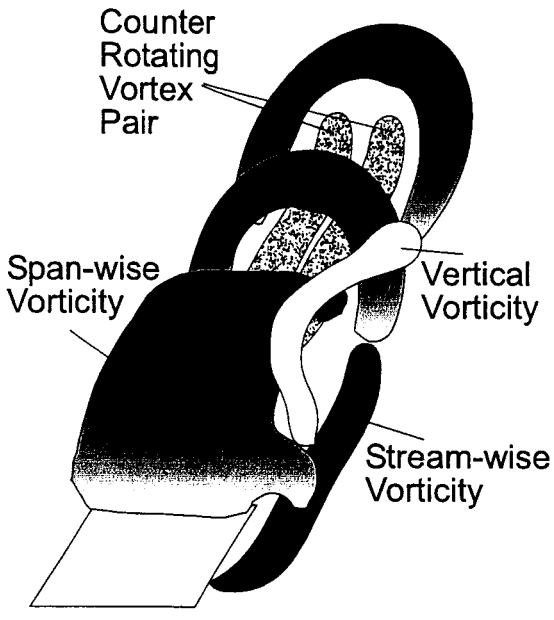

Figure 4.7: Sketch shows the vortex patterns in JICF.

one streamline (originating from one lateral side of the jet) is tracked through the streamwise structure and the axial velocity along this streamline is plotted.

Figure 4.8 (a) shows the location of this streamline and part (b) shows the axial velocity versus distance along the streamline. A sudden "drop" of axial velocity appears at distance of 3.5D, which may be used to identify the location of the vortex break down. In an earlier study of a circular jet in cross flow [56] this breakdown was seen closer to the jet. It is not clear at present if this discrepancy is due to the shape of the jet or some other effect.

The jet side stream-wise structures are lifted into the jet shear layer and therefore, are torn by vertical structures along the jet shear layer, as shown qualitatively in Fig. 4.9. In this figure, jet side stream-wise vorticity is shown in blue and vertical vorticity is shown in red. Part (a) of this figure shows how the vertical structures wraps around the stream-wise vorticity and in part (b) appear to pinch off the streamwise strucure. The detached stream-wise vortex then follows the jet trajectory and creates the necessary background circulation for CRVP.

The vertical structures are also torn during this interaction process, as shown Fig. 4.10. As can be seen from these figures, there is a complex 3D interaction between the shear layers formed along the jet edge and the cross-flow. This interaction results in formation of all three components of vorticity and as the jet bends towards the outflow direction vorticity in one component changes to another. Vortex stretching, breakdown and re-connection of structures occur in this flow field.

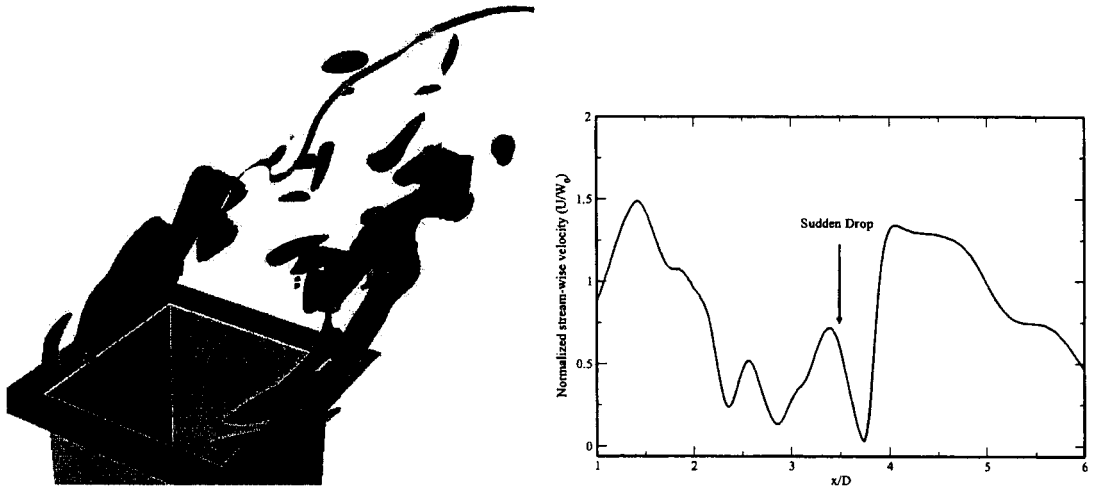

(a) (b)

Figure 4.8: Sudden drop in axial velocity indicates the vortex breakdown. (a) jet-side stream-wise vorticities, blue: +1 and light blue: -1, (b) Velocity as a function of distance along the streamline.

Other flow structures are also present. Span-wise roller wraps and realigns its direction (from span-wise to stream-wise) due to the stronger momentum entrainment at the jet side relative to jet center. Figure 4.11 part (a) shows how the surface of the span-wise roller is skewed and part (b) shows the resulting CRVP from the realignment of span-wise rollers at the corner of the jet.

In order to confirm the vortex realignment, the contour plots for vortices and their stretching components for one shedding cycle of the jet were analyzed and some representative figures are shown in Figs. 4.12-4.14. Figure 4.12(a) shows the span-wise vorticity at time t = 0.2310 (s) at the jet side ($y/d = -0.5$). Also, the span-wise vortex stretching component ($\omega_j \frac{\partial v}{\partial x_j}$) and stream-wise vortex stretching component ($\omega_j \frac{\partial u}{\partial x_j}$) are shown in part (b) and (c), respectively. In the region of $0.5 \leq x/d \leq 1.0$ and $0.3 \leq z/d \leq 0.6$, the span-wise vorticity with the magnitude of 1.48 (see part a) undergoes a span-wise compression (see part b) and stream-wise stretching (see part c). As a result, this span-wise roller at the corner of the jet tilts and combines with the torn stream-wise vorticities.

The span-wise vorticity contours at this time (t + T/2) is shown in Fig. 4.13 (a). The tilted vortex has aligned with x-axis and appears as a stream-wise vorticity as shown in Figs. 4.13 (b) and (c) in top and side views. In these views, such vortex is recognizable at about x/d = 1.0, y/d = -0.5 and z/d = 0.5. The formation of the CRVP is seen in the streamwise vorticity at x/D = 1.0. The CRVP is convected downstream and its strength changes with time and location. For instance, the CRVP at two other locations of x/d = 0.5 and 3.0 are shown in Figs. 4.14 (a) and (b), respectively. Signification three dimensionality and interaction of the vortices can be

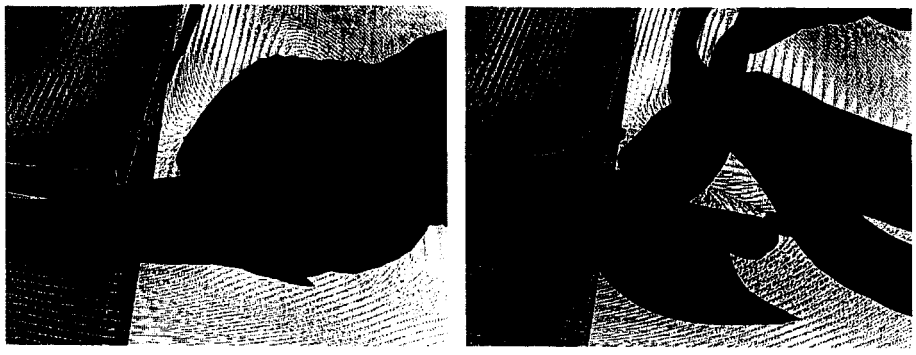

(a) t = T/6 (b) t = 5T/6

Figure 4.9: Jet-side stream-wise vorticities (Blue) and vertical structures (Red) for R = 1.

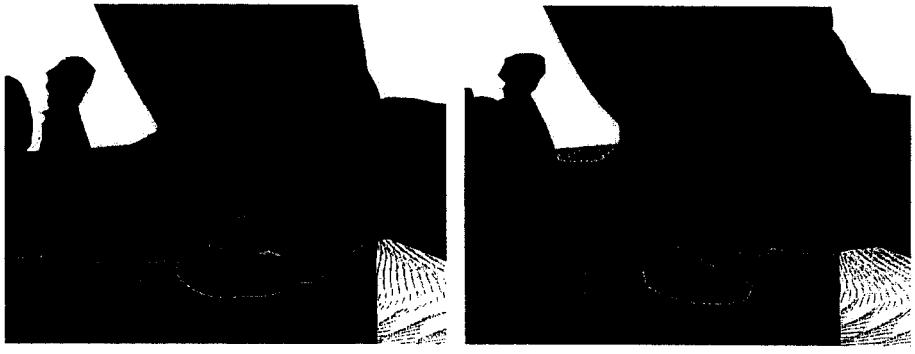

(a) t = T/2 (b) t = 2T/3

Figure 4.10: Jet-side stream-wise (Blue) and vertical structures (Red) for R = 1.

(a) t (b) t + T/2

Figure 4.11: Span-wise vorticity shedding and its contribution to CRVP.

seen in these figures. The lift-off the CRVP is also observable further downstream of the jet injection location.

4.1.4 Mean Flow

The mean stream-wise velocity profile are presented for $R = 0.5$ at various stream-wise stations (x/d= 0, 1, and 5) along the jet center plane, $y/d = 0$ in Figs. 4.15(a-c), and along the jet edge plane, $y/d = -0.5$ in Figs. 4.15(d-f). The current LBE-LES results are compared with experimental data and the past numerical predictions using various RANS closures [32]. At $x/d = 0$, which is the core of the jet, the crossflow is clearly dominant. Further downstream at $x/d = 1$ a region of recirculation is evident in the center plane but is not evident at the edge of the jet, suggesting that the recirculation is confined primarily in the shadow of the jet. This is understandable since the crossflow is flowing around the jet and provides a confinement effect. These observations are consistent with measurements, although the transverse extent (in the z-direction) of the reverse flow is somewhat under-predicted by all numerical results. Away from the wall (e.g., $z/d > 1$), the agreement between all numerical results with data is quite good.

Further downstream axially ($x/d = 5$), the core flow shows two distinct profiles: a near-wall nearly uniform profile for $z/d < 1$ which may be the jet that has attached to the wall and a far field boundary layer like profile for $z/d > 1$ which may be attributed to the crossflow.

The mean wall-normal velocity profiles along the jet center plane and along the jet edge are shown in Figs. 4.16(a-c) and 4.16(d-f), respectively. For this case, the jet penetration is limited to $z/d < 1$ (Fig. 4.16a). Further downstream ($x/d > 1$) the jet motion normal to the wall is significantly reduced since the jet is now getting turned in the axial direction by the crossflow. The agreement in general, is reasonable close to the jet orifice and also for $z/d > 1$ at all locations. There are, however, discrepancy further downstream ($z/d = 5$) in the peak values. The very near-wall region ($z/d < 0.25$) is not well resolved by all models; however, LBE-LES appears to capture the experimentally observed small negative values near $z/d = 1$ (Fig. 4.16). In this region, the flow is turning back towards the wall as the jet is turned down and attaches to the wall.

Figures 4.17(a) and (b) show the computed and experimental contours of the normalized mean stream-wise velocity, U/W_j at axial location $x/d = 1$, respectively for R = 1 case. Although the exact shape is not the same the overall features are in good agreement, including the small negative velocity in the core.

4.1.5 RMS and Turbulent Properties

Turbulent kinetic energy (TKE) profiles along the jet center plane at various axial locations are shown in Figs. 4.18(a-c), respectively. In LBE-LES, the TKE is obtained by time-averaging the resolved kinetic energy and then removing the mean kinetic energy, whereas, in the RANS approaches TKE is a modeled quantity. TKE is produced not only during interaction between the crossflow boundary layer and

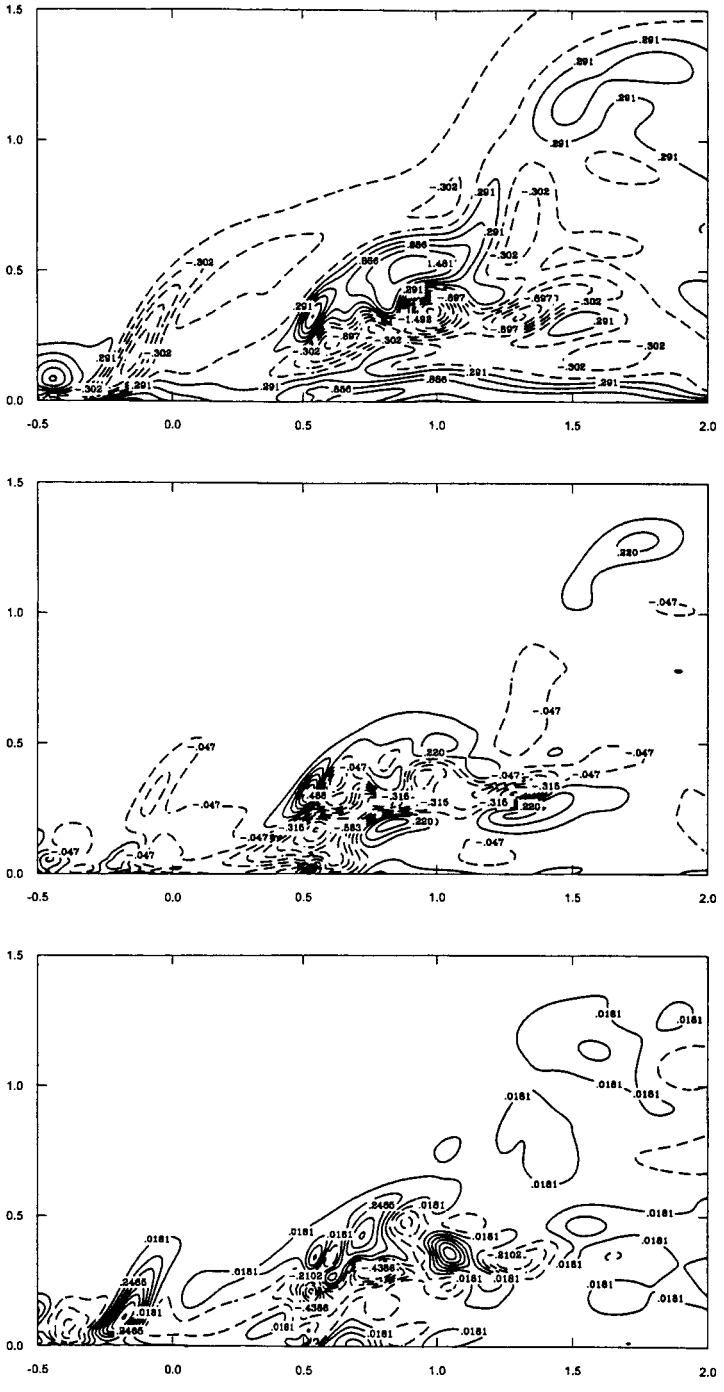

Figure 4.12: Vortex tilting at y/d = -0.5, time t.
(a) Span-wise Vorticity, (b) span-wise stretching, and (c) stream-wise stretching.

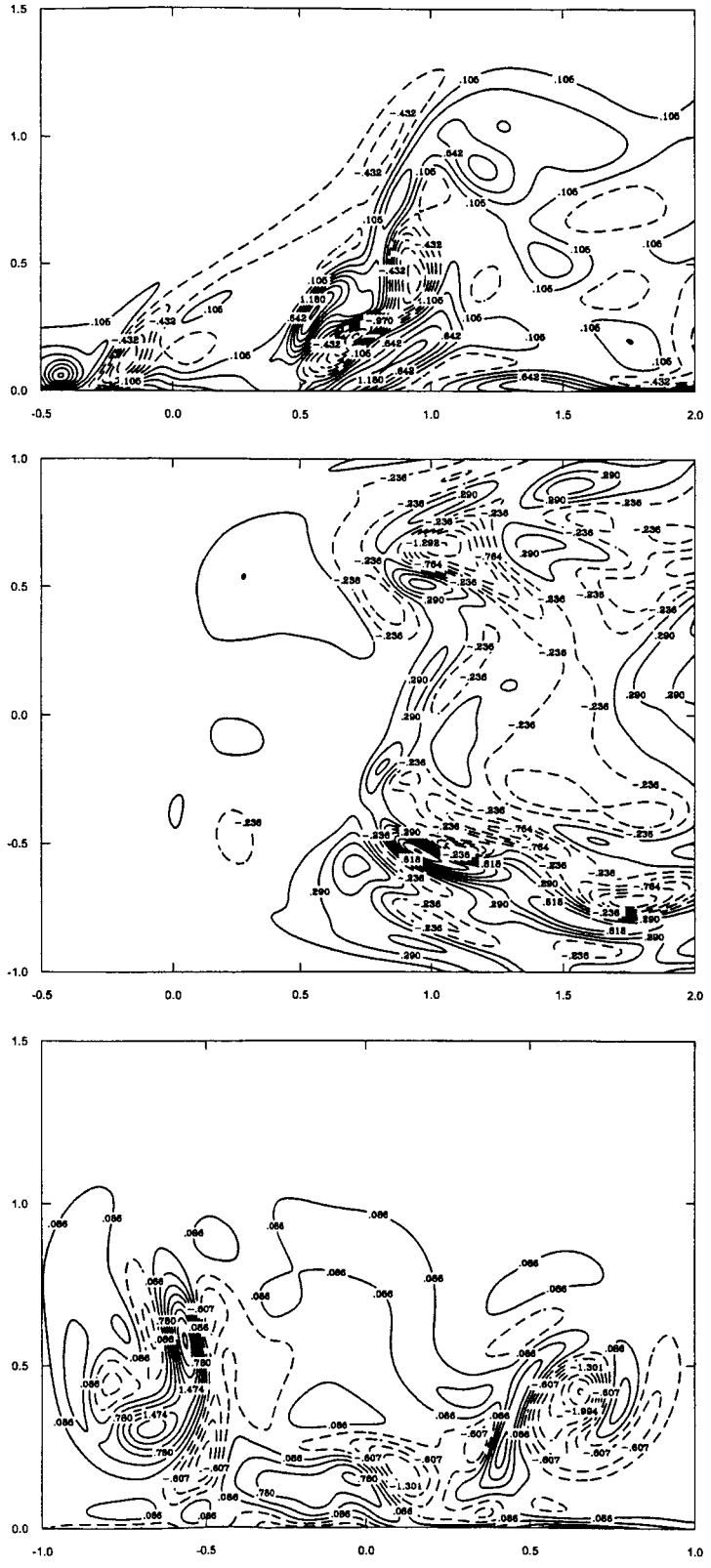

Figure 4.13: Span-wise and stream-wise vorticities at time t + T/2. (a) Span-wise vorticity at y/d = -0.5, (b) stream-wise vorticity at z/d = 0.50, (c) stream-wise vorticity at x/d = 1.0.

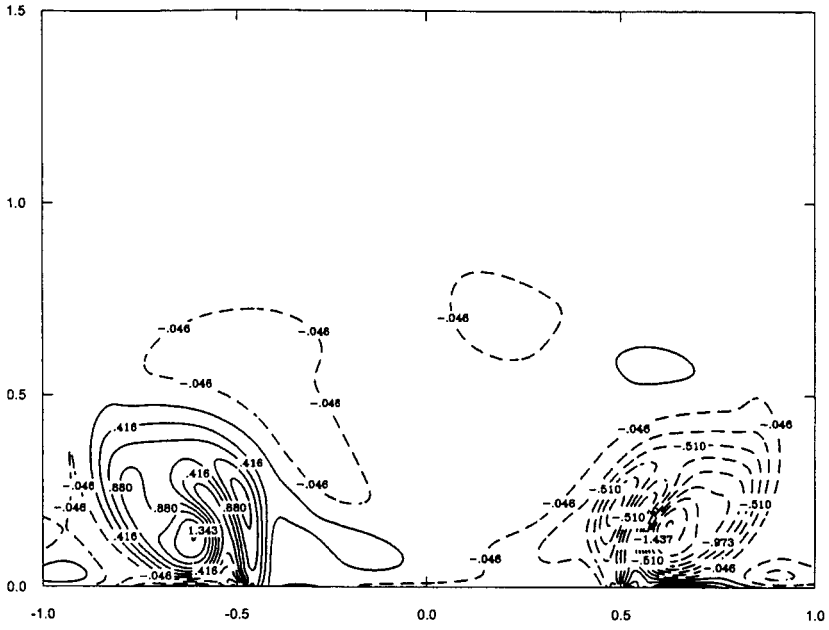

(a) x/d = 0.5

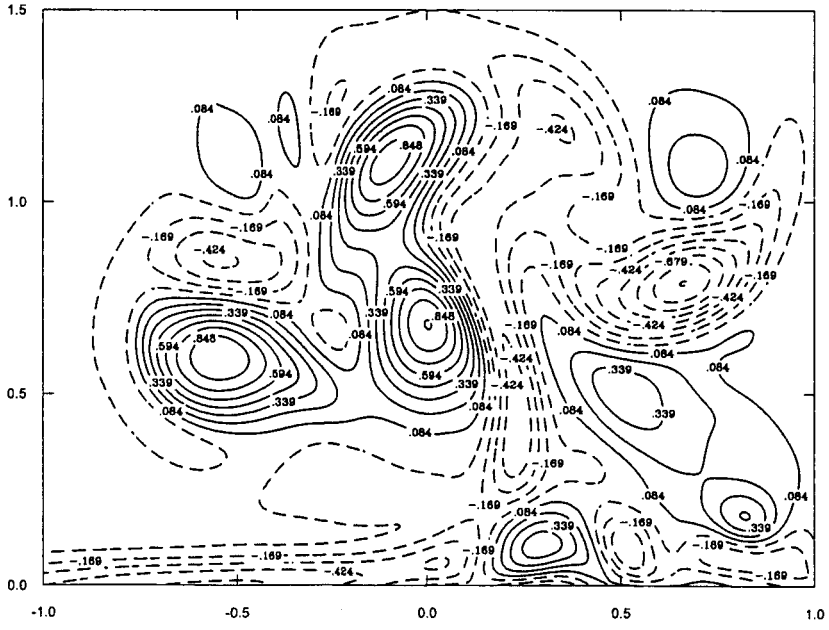

(b) x/d = 3.0

Figure 4.14: Stream-wise vorticity at time t + T/2.

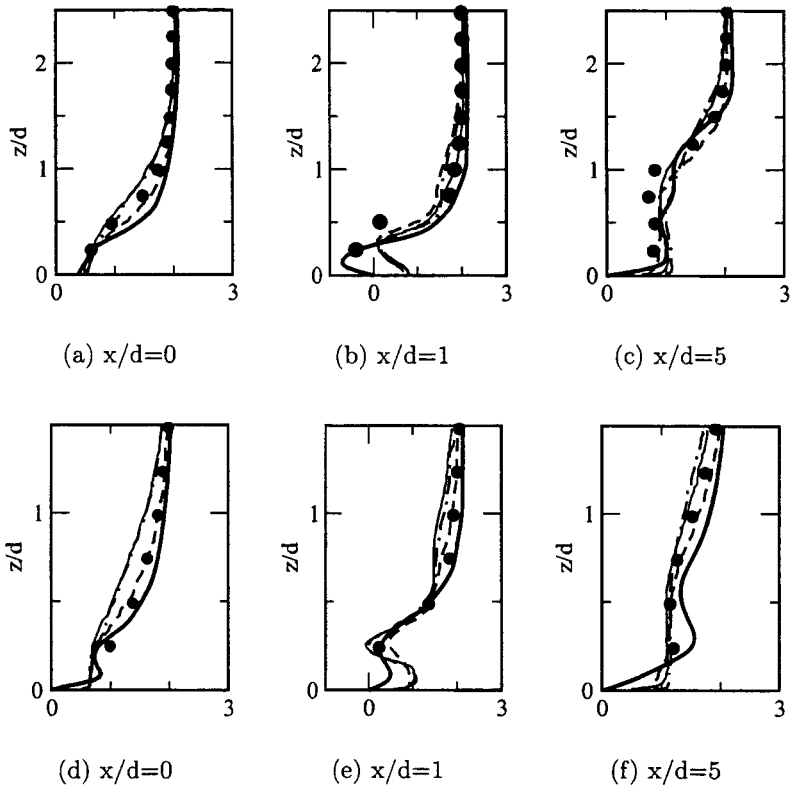

Figure 4.15: (a-d) Mean stream-wise velocity profiles (U/W_j) along the jet center plane $y/d = 0$ at $x/d = 0$, 1, and 5 from the jet center (R = 0.5). (e-h) Mean stream-wise velocity profiles (U/W_j) along the jet edge plane $y/d = -0.5$ at $x/d = 0$, 1, and 5 from the jet center (R = 0.5).

- $-\cdot\cdot$ RST using Chen (1995) model (Hoda, 2000)
- • Experimental data (Ajersch, 1997)
- $--$ RST using Lam-Bremhorst model (Hoda, 2000)
- — RST using Launder-Tselepidakis model (Hoda, 2000)
- — SRT-LBE-LES using dynamic Smagorisky model

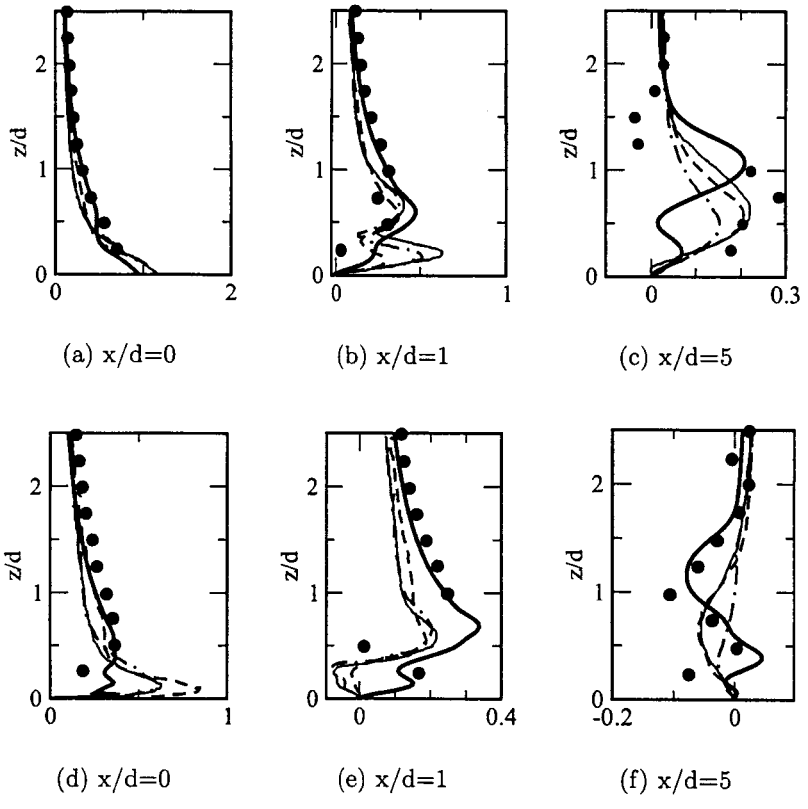

Figure 4.16: (a-c) Mean wall-normal velocity profiles (W/W_j) along the jet center plane $y/d = 0$ at $x/d = 0$, 1, and 5 from the jet center (R = 0.5). (d-f) Mean wall-normal velocity profiles (W/W_j) along the jet edge plane $y/d = -0.5$ at $x/d = 0$, 1, and 5 from the jet center (R = 0.5).

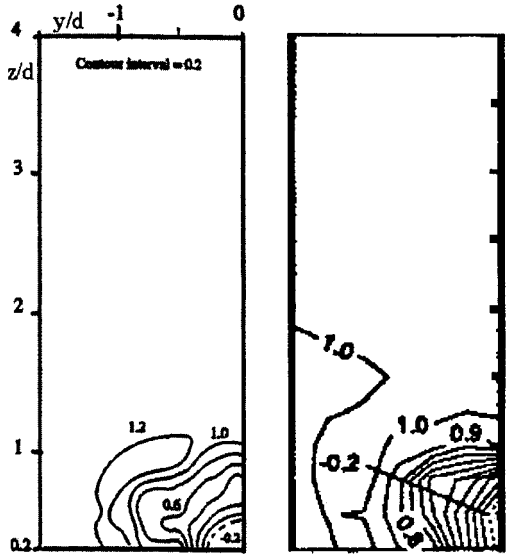

(a) LBE Results (b) Exp. data

Figure 4.17: Comparison of LBE results with experiment for R=1. Normalized stream-wise velocity $\frac{U}{W_j}$ at $x/d = 1$.

the jet, but also due to various velocity gradients and strong streamline curvature. Peak of TKE profile is located at the location of maximum velocity gradients. TKE is larger at the top of the jet where the interactions are dominant (see discussion on coherent structures above). Comparison (not shown) of turbulence fluctuation intensity in the stream-wise (u_{rms}/W_j) and wall-normal (w_{rms}/W_j) directions shows that these fluctuation levels are similar in magnitude but that there are significant anisotropy in the near-wall region. This is to be expected since in this region vortical breakdown occurs in a complex 3D manner.

Figures 4.19 (a-c) shows the normalized shear stress ($\overline{uw}/W_j$) profiles along the centerline at various axial locations. Although the general trend is similar to the experiment, the LES-LBE prediction is significantly larger in many regions. There are two possible reasons for this. In general, the Reynolds stress prediction in highly separated flow regions is very difficult and the algebraic subgrid closure used here may not be appropriate. Another possible reason is that in LES higher order moments typically take much longer to reach statistically stationary state and the current simulation may not have been run long enough (although around 4 flow-through-times have been averaged for the current data). Improved non-equilibrium subgrid model, such as the localized subgrid kinetic energy model [24] and longer statistical averaging may improve this prediction and will be addressed in the future.

The comparison between LBE-LES and experiment of the cross-stream ($y - z$) contours of the mean TKE and Reynolds stress ($\overline{uw}/W_j^2$) are shown in Figs. 4.20(a,b) and Figs. 4.20 (c,d), respectively. For direct comparison, the same contour interval is

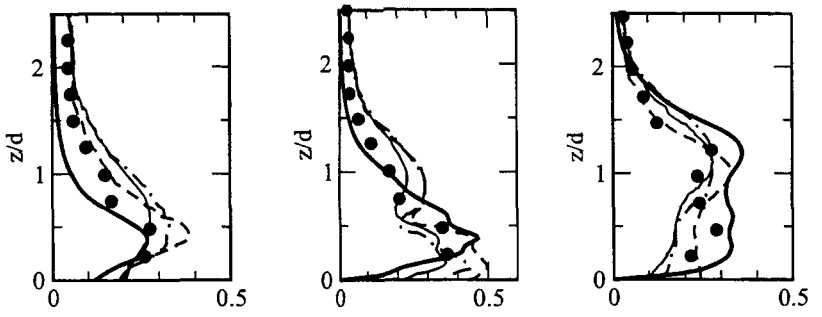

Figure 4.18: Mean turbulence kinetic energy $\sqrt{k}/W_j$ along the jet center plane $y/d = 0$ at $x/d = 0$, 1, 5 from the jet center (R = 0.5).

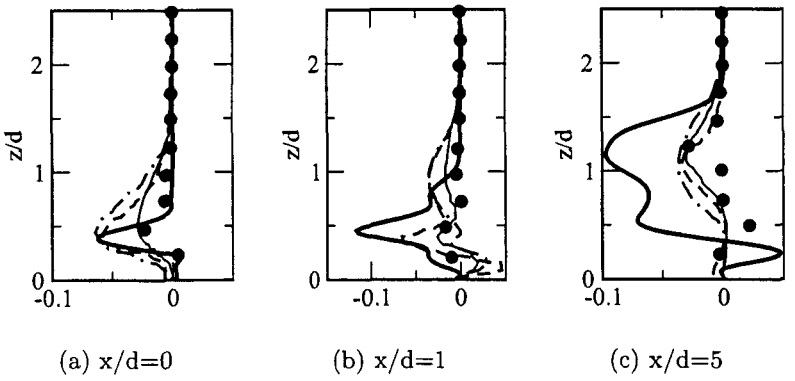

Figure 4.19: Turbulence shear stress uw/W_j^2 profiles along the jet edge plane $y/d = 0$ at $x/d = 0$, 1, and 5 from the jet center (R = 0.5).

used. In general, there is reasonable agreement between the two studies. The location and magnitude of both TKE and Re-stress are well predicted in the current LBE-LES study. The normalized contours of the Re-stress $v\tilde{w}/W_j^2$ shown in Figs. 4.20 (e,f) compares the predictions with measurements. Again, there is good agreement with data.

4.1.6 Comparison of SRT and MRT Results

To avoid oscillations near the sharp corners due to the geometrical singularities at these locations, the multiple relaxation time method has been developed in the past [32]. Such method eliminates the strong local spatial oscillations and improves the stability of the LBE scheme. In the past, comparison between SRT and MRT results are done for Stokes first problem, steady uniform flow over finite/semi-finite plate and cavity flow [32]. These results suggest that MRT model is better behaved in flows involving large gradients and high Re numbers. The Re number for the jet-in-cross flow simulation presented here, is about 4700 and large oscillations were not seen for SRT simulation. In fact, as shown in the previous section, the SRT model is quite capable of capturing most of the features of interest in the JICF for the cases simulated here. However, in order to ensure the accuracy of the results, two cases of R = 0.5 and 1.0 were also simulated using MRT model and results were compared with SRT as well as experimental values. No major difference between SRT and MRT results were seen. Some results and included here for completeness.

Results at $x/d = 1$ along the jet center and jet edge planes are shown in Fig. 4.21. This location ($x/d = 1$) was chosen for comparison since it was at the vicinity of the sharp edges and the most likely place where results could differ. Figures 4.21(a) and (b) show respectively, the stream-wise velocity at the jet center and edge planes, and compares them to the SRT results. The scatter between MRT and SRT is negligible for this test case.

Figure 4.21(c) and (d) show the wall normal velocity at center and edge jet planes and Figs. 4.21(e) and (f) show the mean turbulent kinetic energy and uw shear stress along the jet center plane. Again, it can be seen that there are not that significant differences seen between the two methods, at least for this test case.

Nevertheless, based on past studies, it is very likely that the MRT LBE model is probably the more robust one and should be used for high Re test cases.

4.2 Hybrid FV-LBE-LES Solver Validation

In this section, we first test the boundary information exchange in the coupling between the two solvers by passing an acoustic pulse from each domain, and then describe the coupled simulation of JICF case discussed above to complete the validation process.

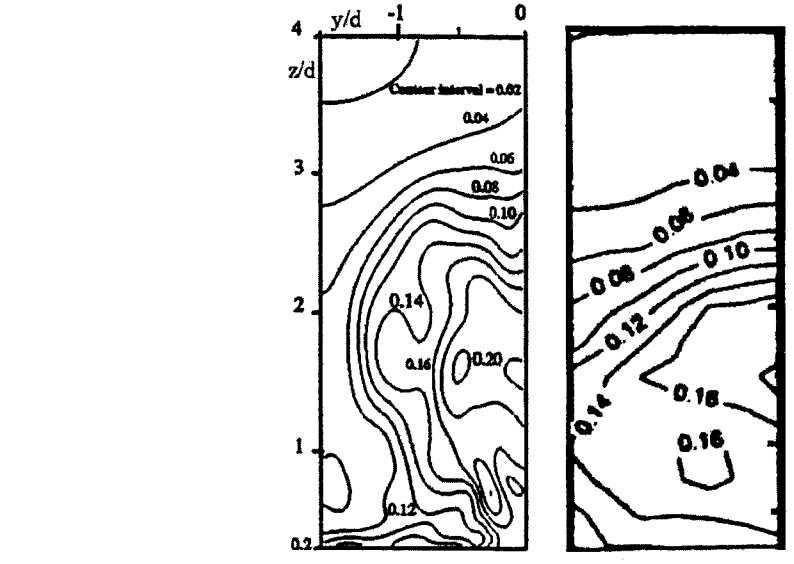

(a) LBE Results (b) Exp. data

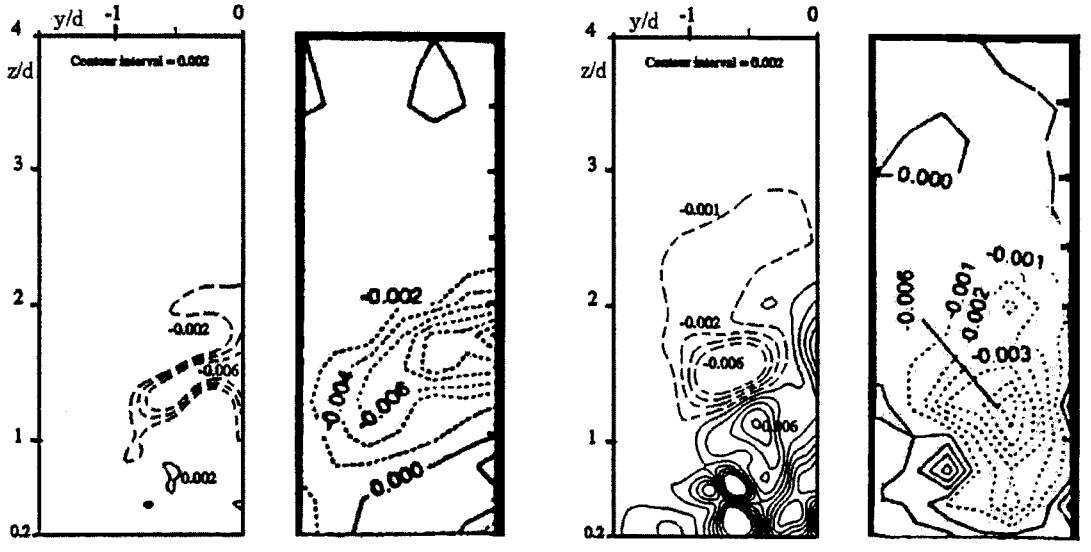

(c) LBE Results (d) Exp. data (e) LBE Results (f) Exp. data

Figure 4.20: Comparison of LBE results with experiment for R = 1. (a,b) Normalized TKE $\frac{\sqrt{k}}{W_j}$ at $x/d = 8$, (c,d) Normalized shear stress $\frac{\bar{uw}}{W_j{}^2}$ at $x/d = 5$, (e,f) Normalized shear stress $\frac{\bar{vw}}{W_j{}^2}$ at $x/d = 5$

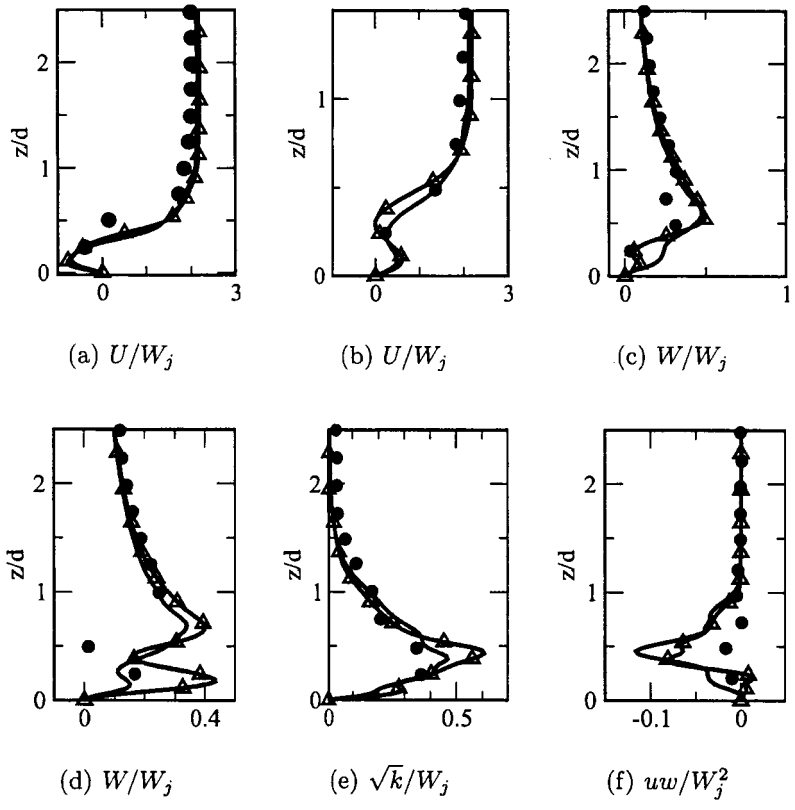

Figure 4.21: Multiple-relaxation-time results for R = 0.5 shown with triangles on top of single-relaxation time results shown with solid lines. (a,b) Mean stream-wise velocity along the jet center and edge planes, (c,d) Mean wall normal velocity along the jet center and edge planes, (e) Mean turbulent kinetic energy along the jet center plane, (f) Turbulence shear stress profiles along the jet edge plane.

4.2.1 Acoustic Pulse Test

The behavior of the coupling scheme at the boundaries is examined using acoustic wave test. This type of test is used in many codes to evaluate the proper implementation of boundary conditions. In the first case of interest, the LBE to FV coupling is tested. An acoustic pulse, is initially generated in LBE domain, propagating toward FV domain. The acoustic pulse was is created at $t = 0$ by using the initial conditions:

$$U^* = U_0^* + A \exp\left(-\left(B\frac{x^* - L^*/2}{L^*}\right)^2\right)$$

$$Q(1) = 1 + (U_0^* - U^*)$$

where $U_0^* = 0$, $A = 0.01$, and $B = 15$ are considered. Figure 4.22 shows the velocity, density and pressure variation along the stream-wise direction. The amplitude and the wave length of the pulse remains constant as it passes through the coupling boundary which proves the validity of the coupling approach when information are sent from LBE to NS domain.

The characteristic velocity for LBE is 0.05 and is equivalent to 10.15 m/sec for FV formulation. Also the characteristic length for LBE is 80 which is equivalent to 0.01 (m). Equivalent velocity and length for FV domain are determined by matching the Re number. The computational grid for LBE and FV domains are 80X20X20 each. This case is setup in such a way that time step for the LBE is equal to time step for FV scheme. The time step for LBE scheme is computed as:

$$\delta t_{lbe} = \frac{\delta_x}{c_r} = \frac{0.000125}{203} = 0.5 \times 10^{-6}$$

$$\delta t_{les} = CFL * () = 0.5 \times 10^{-6}$$

Finally, the transfer from the FV to the LBE is tested by generating the acoustic wave inside of the FV domain, which propagates toward LBE domain. The initial conditions at $t = 0$ are set as:

$$u = u_0 + A \exp\left(-\left(B\frac{x - L/2}{L}\right)^2\right)$$

$$p = p_0 + \rho_0 c_0 (u - u_0)$$

$$\rho = \rho_0 + \frac{\rho_0 (u - u_0)}{c_0}$$

$$T = \frac{p}{\rho R_{gas}}$$

where $u_0 = 10.15(m/s)$, $A = 4$, $B = 6$, $p_0 = 101325(pa)$, $c_0 = \sqrt{\gamma R_{gas} T_0}$, $\gamma = 1.4$, $T_0 = 300(K)$, R_{gas} is the gas constant.

Figure 4.23 shows the velocity, density and pressure variations along the stream-wise direction. The amplitude and the wave length of the pulse remains constant as it passes through the coupling boundary which proves the validity of the coupling approach when information is sent from the FV to the LBE domain.

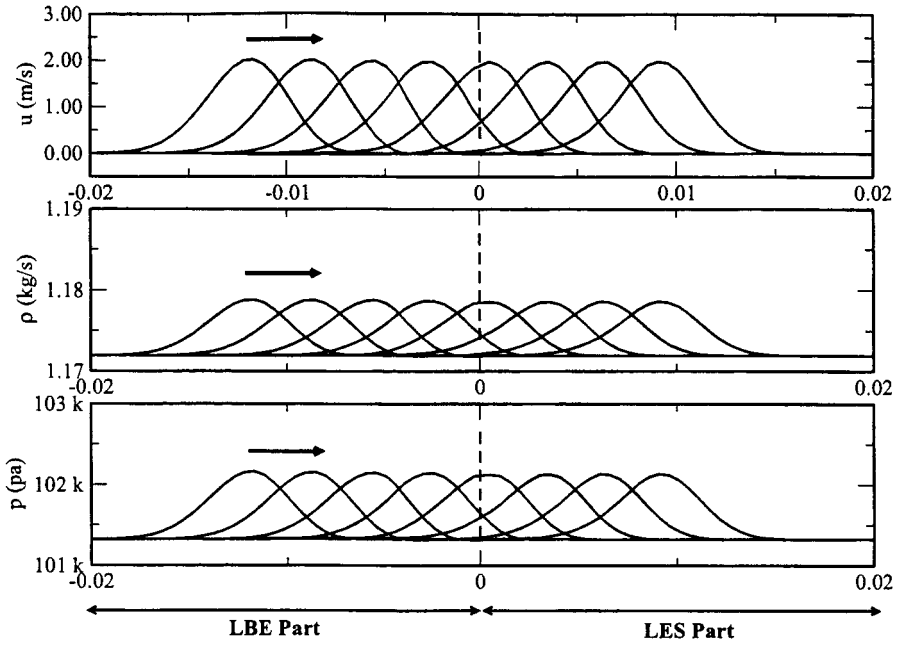

Figure 4.22: Acoustic pulse from the LBE domain to the FV domain

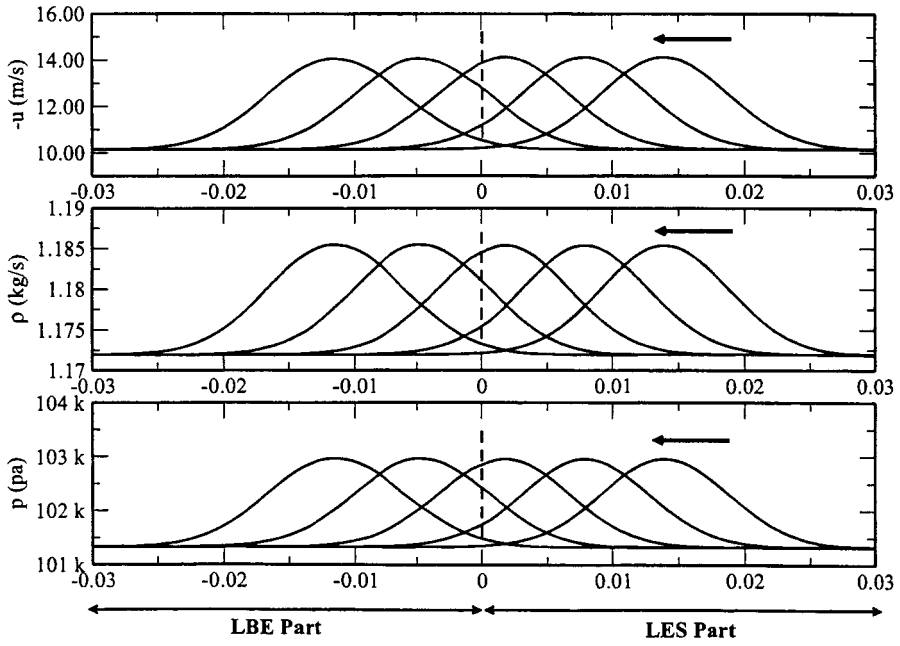

Figure 4.23: Acoustic pulse from the LBE domain to the FV domain

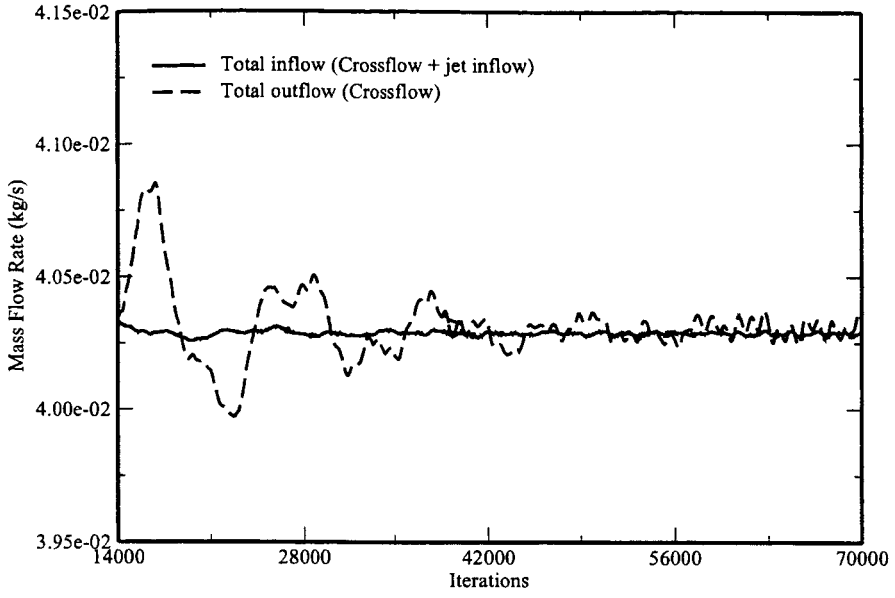

Figure 4.24: Mass conservation validation.

4.2.2 Single Jet in Crossflow

In this study, the experiment of Ajersch *et al.* [51] is again chosen as the benchmark case for validation. The dimensions of the computational domain are shown in Fig. 4.1. The simulation is carried out at Reynolds number of 4700 (based on the jet velocity and the nozzle width D) and at a jet-cross-flow velocity ratio of 0.5. The cross-flow velocity profile is initialized with a boundary layer thickness of $5D$. The computational domain is resolved using $128 \times 96 \times 64$ for the cross-flow domain (FV-LES) and $20 \times 20 \times 100$ for jet section (LBE). So a total of 0.82×10^6 grid points is used to discretize the complete domain. The results from these simulations are compared with the earlier results obtained using the LBE-LES for the *entire* domain [12].

Computation of a full simulation requires approximately 1155 single-processor hours with 1.5GB memory on the IBM SP4 machine. Same boundary conditions as for single JICF in LBE simulation were specified here as well.

Results are compared with the experiment of Ajersch and the earlier full LBE-LES simulation. Comparison of LBE-LES with numerical results of Hoda *et al* [52] were discussed earlier and it was shown that the full LBE-LES approach can capture with reasonable accuracy the experimental mean and rms velocity profiles. Therefore, we only compare the current LBE-FV-LES coupled results against the earlier LBE-LES results.

All the important features in JICF such as the horse-shoe (or kidney-shaped) structure and counter rotating vortex pair (CRVP) observed in earlier LBE-LES (and in the experiments) are captured in the present simulation with reasonable accuracy (and in very good agreement with the previous study).

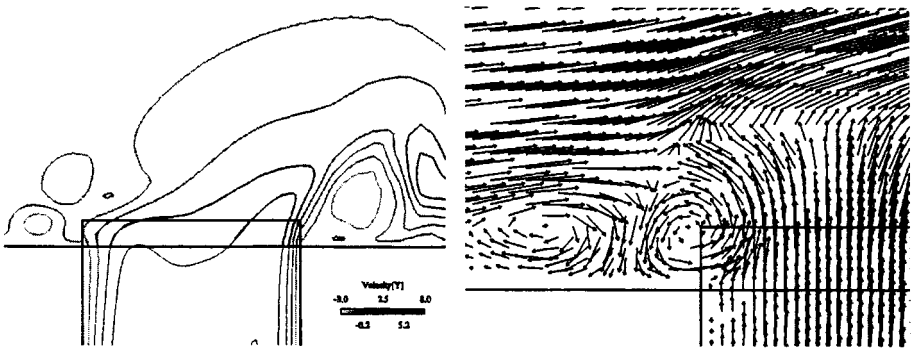

(a) (b)

Figure 4.25: Velocity contours shows the flow in the recirculation zone and the motion downstream.

Mass conservation of the inflow and outflow is shown in Fig. 4.24 to demonstrate that this coupled simulation approach can conserve mass. The velocity contours in Fig. 4.25 shows the formation of the recirculation zone behind the jet. By reviewing time evolution of the flow field it is seen that the recirculation bubble periodically sheds the flow in-phase with the motion of the kidney-shaped vortices observed in this flow.

The periodic shedding of the flow from the recirculation zone is show more clearly in Fig. 4.25 which shows the velocity contours along stream-wise direction. Smooth transition of velocity contours from LBE domain to NS domain shown in this figure clearly demonstrated the accuracy of the LBE-NS coupling employed in the present approach.

The mean velocity profiles comparison with past LBE-LES and experimental data at representative stream-wise stations ($x/D = 0, 1, 3$) along the jet center plane ($Y/D = 0$) is shown in Figs. 4.26 (a-i). The exit plane velocity is well captured by LBE-LES and the reverse flow at $X/D = 1$ is also captured. Turbulent profiles at the jet center plane are shown in Figs. 4.27(a-i) which also shows good agreement with experiment.

4.2.3 Parallel Performance and scalability of the Hybrid Solver

The overall performance of the coupling algorithm is determined for the above JICF case. The test grid resolution of 72x64x60 & 25x25x50 for crossflow and jet sections are considered in this study. So the total of 300k grid points, which require 1.07 Gbytes memory are solved on a IBM/SP4 platform to obtain this scaling data.

Table 4.2 lists the timing results for four cases with different number of processors. In this table, the total wall time per step, scalability and the ratio of number of grids in each processors of FV domain to the number of grids in each processors of LBE domain are given.

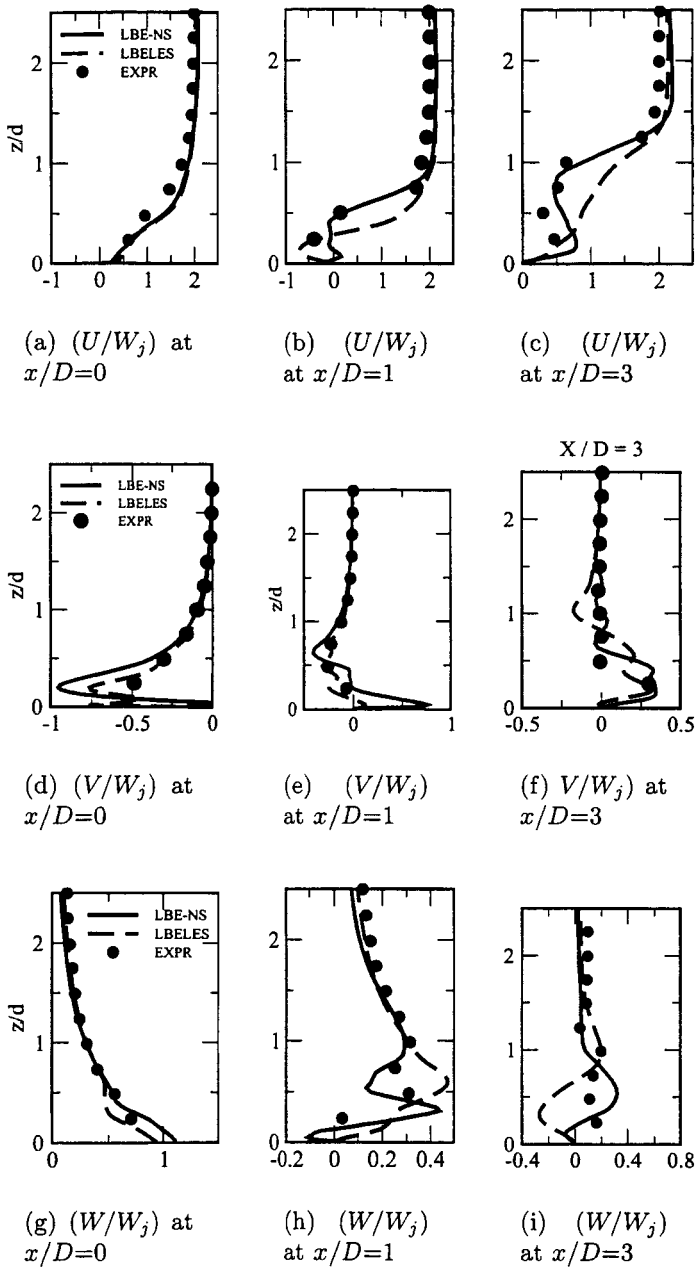

(a) (U/W_j) at x/D=0 (b) (U/W_j) at x/D=1 (c) (U/W_j) at x/D=3

(d) (V/W_j) at x/D=0 (e) (V/W_j) at x/D=1 (f) $V/W_j)$ at x/D=3

(g) (W/W_j) at x/D=0 (h) (W/W_j) at x/D=1 (i) (W/W_j) at x/D=3

Figure 4.26: Mean velocity profiles along the jet center plane (y/D=0) at x/D=0, 1, and 3 from the jet center.

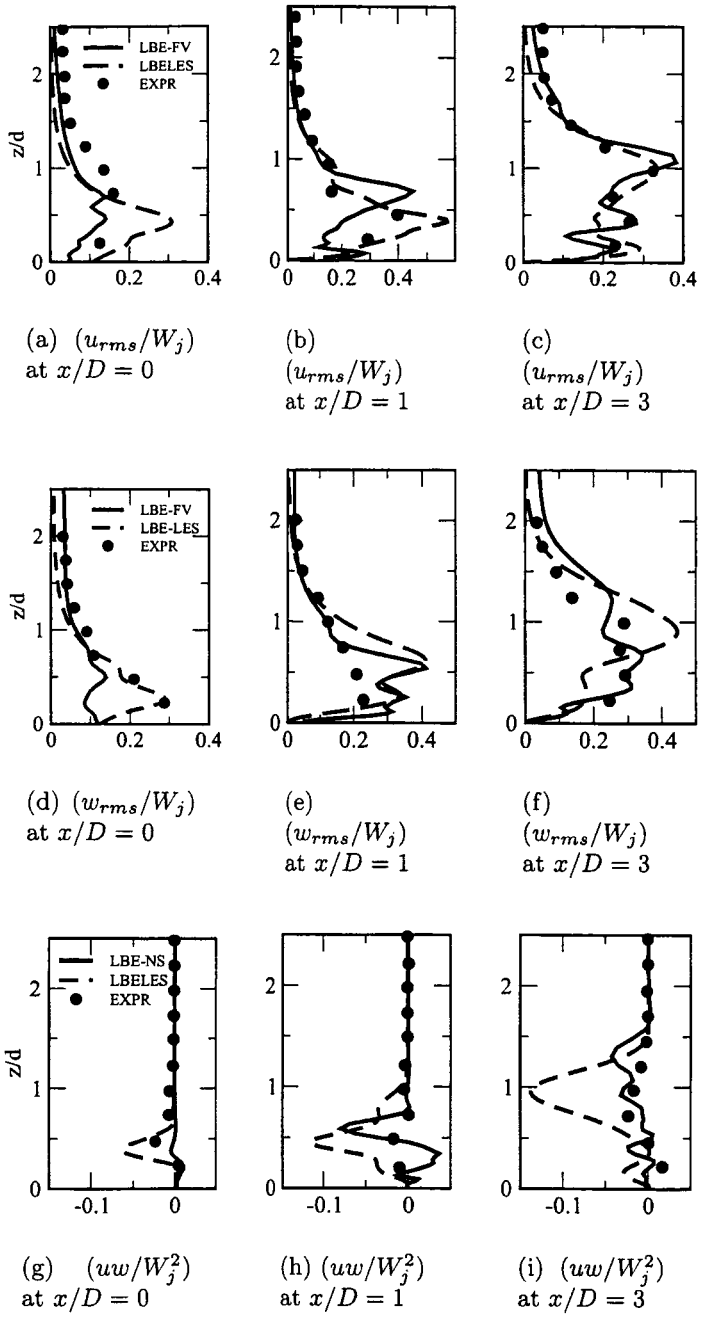

Figure 4.27: Turbulent profiles along the jet center plane (y/D=0) at x/D=0, 1, and 3 from the jet center.

Case #	1	2	3	4
Number of CPU's (FV + LBE)	5 (4+1)	9 (8+1)	17 (16+1)	31 (30+1)
Run-time/step (secs)	0.76	0.38	0.25	0.23
Scalability (T_{base}/T_N)	1.0	2.0	3.0	3.3
Grid ratio (FV/LBE)	3.0	1.5	0.7	0.4

The scalability is defined as T_{base}/T_N where T_{base} is the run time on N_{base} processors and T_N is the run time on N processors.

Table 4.2: Coupled scheme performance and scalability on a IBM/SP4 for the single JICF validation case with a resolution of 300K grid points. N_{base}=4 and T_{base}=12.8 (min.).

Case #	3
Number of CPU's	17
Run-time/step (secs)	1.21
Parallel cost(% of run time)	14.9
Cost for FV domain (% of run time)	80.1
Cost for LBE domain (% of run time)	5.0
Scalability	3.0

Table 4.3: Computational cost for the single JICF validation case with a resolution of 300K grid points.

A performance analysis for case #3 is carried out in order to measure the parallel overhead and the cost of each subroutine in the coupled algorithm. Table 4.3 summarizes the percentage of run time for the Navier-Stokes solver, LBE solver and parallel communication. As expected FV domain takes the majority of the run time, i.e. 80%, since it solves 7 finite-volume differenced equations on a large grid. The LBE only solves for the advection equation (along 18 directions) on a relatively small grid size with a cost of 5 percent of run time. The parallel cost is large at about 15% due to the communication time between the two domains, as well as the communication time for the solvers themselves.

4.3 Multiple Micro-Jets in Cross-flow

This section reports on the fully coupled LBE-FV-LES simulation of turbulent multiple micro-jets in crossflow. Earlier micro-hole matrix of different combinations were simulated. Here, we report on a representative case of a matrix of 3 x 3 micro holes in a high Mach number turbulent boundary layer. This test case is similar to the experiment at NASA/GRC [4] except that only a 3 x 3 matrix is simulated, whereas in the experiment, thousands of micro holes on a large flat plate were employed. Our present effort is to demonstrate this coupled approach.

In the micro blowing technique experimentally investigated at NASA/GRC [4], a plate with porosity of 13 to 43 percent was studied and it was shown that drag can be significantly reduced. Holes diameters ranged from around 0.2 to 0.5 millimeter and

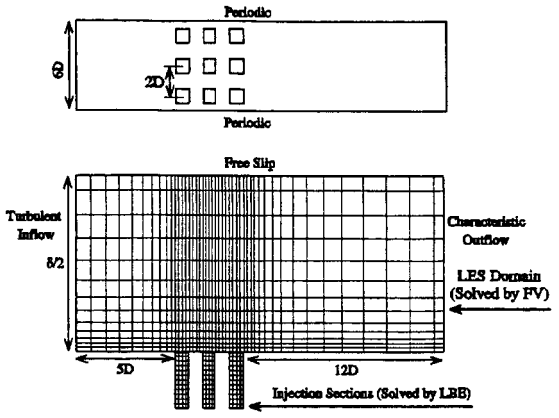

Figure 4.28: Geometry and grid configuration for multi hole simulation (every five grid is shown).

depending on plate porosity, an order of 100000 micro holes existed on a $100cm^2$ flat plate area. Simulation of flow inside such tiny holes along with a cross-flow domain whose length scale is orders of magnitude larger is a challenging problem.

Here, we simulate a 3 x 3 square pattern of injection holes each with diameter of $D = 0.5mm$ and equally spaced a distance of D apart, as shown in Fig. 4.28. Turbulent inflow profile is specified $5D$ upstream of injection holes with a free stream velocity of $U_0 = 138.54m/s$ and boundary layer thickness of $\delta = 12mm$. These conditions closely approximate the experimental data. Slip boundary conditions is imposed on the upper plane at a distance $\delta/2$ above the injection holes, and characteristic outflow conditions were imposed at a location $12D$ downstream of the holes. Periodic boundary conditions are imposed in the spanwise direction.

The plate porosity is defined by cumulative hole area divided by the plate area. For our test case here it is 25%. The blowing rate $(V_{jet}/U_0))$ of 0.006 is simulated here. The holes have an aspect ratio (L/D) of 4 and the hole inflow velocity profile is specified as:

$$V_{inflow} = V_{jet} sin(\frac{\pi x}{D}) sin(\frac{\pi y}{D}).$$

Based on the experiments done at NASA/GRC, the flow conditions are set as following. The tunnel pressure is 0.24 atm and the density, the kinematic viscosity and the Reynolds number per meter are found as,

$$\rho = \frac{P}{RT} = \frac{24318}{(287)(300)} = 0.28(kg/m^3),$$

$$\nu = \frac{\mu}{\rho} = \frac{18.48 \times 10^{-6}}{0.28} = 66.0 \times 10^{-6}(m^2/s)$$

$$Re = \frac{Vx}{\nu} \Longrightarrow \frac{Re}{x} = \frac{138.0}{66.0 \times 10^6} = 2.1 \times 10^6(/m)$$

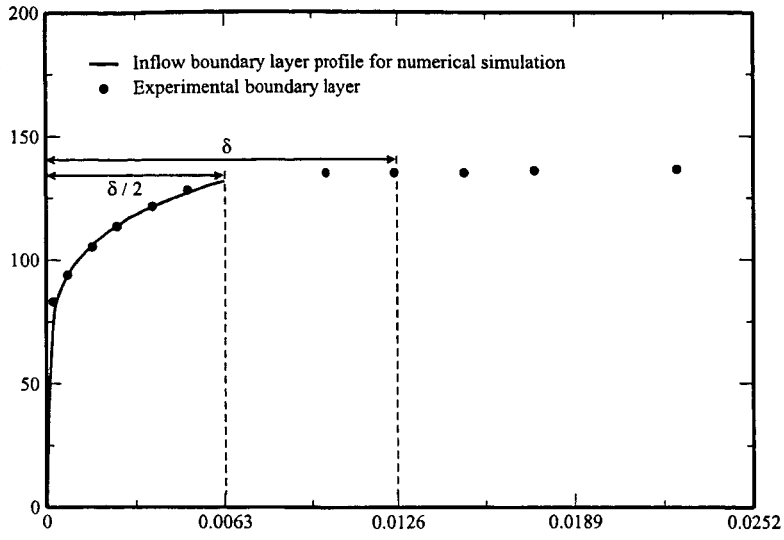

Figure 4.29: Inflow boundary layer profile imposed for numerical simulation which matches the inflow BL measured in the experiment.

Since the leading edge of the test plate in the experiment is 25.4 cm downstream from the end of wind tunnel transition duct, the Re number at the leading edge of the test plate is found as,

$$x_{start} = 0.254(m) \Longrightarrow Re_x = 0.55 \times 10^6$$

Using this information, the momentum thickness Re can be calculated,

$$Re_\theta = 0.045 {Re_x}^{0.79} = 2683$$

which gives the momentum thickness of $\theta = 0.0012m$. The boundary layer shape factor measured in the experiment is equal to $H = 1.34$, and thus the theoretical friction coefficient is computed [57] as,

$$C_f = 0.246.10^{-0.678H} (\frac{Re_\theta}{H})^{-0.268} = 0.0039$$

In addition, the theoretical boundary layer thickness can be determined from the shape factor and the momentum thickness using the following relation,

$$H = 1 + \frac{2}{n} = 1.34 \Longrightarrow n = 5.88$$

$$\frac{\theta}{\delta} = \frac{n}{(n+1)(n+2)} = 0.1084 \Longrightarrow \delta = 0.0126$$

Using this information, a turbulent inflow boundary layer is created for the numerical simulation and shown in Fig. 4.29. In this graph the theoretical boundary layer thickness is highlighted.

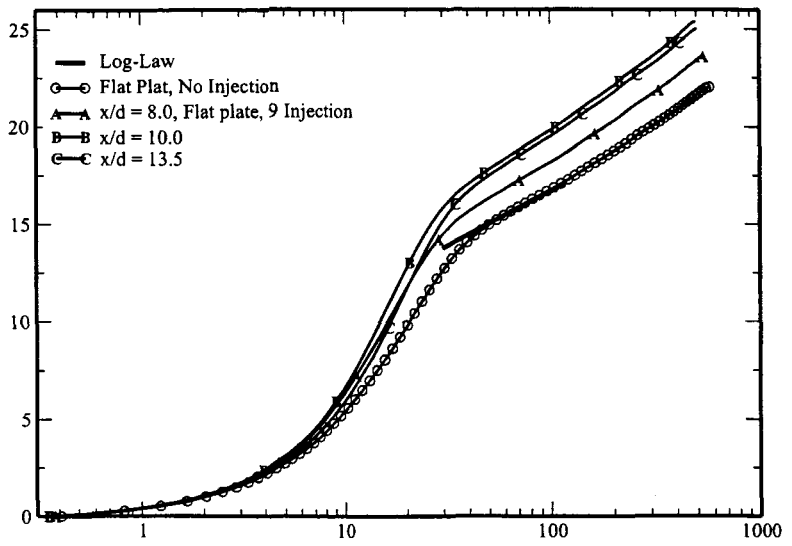

Figure 4.30: Time averaged velocity profile at the inflow based on the wall coordinate.

This inflow is generated in such a way that agrees with the Log-law profile as well. Figure 4.30 depicts the time averaged velocity profile based on wall coordinate. The log law profile is shown in this graph as well for comparison.

Figure 4.31 shows the boundary layer profile at different stream-wise locations along the plate in-between the injection holes. It can be seen that even this small blowing can result in the change in the boundary layer profile in the inner layer ($y/\delta \leq\leq 0.03$).

Since the injection starts at $x/D = 5$, the friction velocity decreases past this location, and once the injection stops (at $x/D = 11$), it begins to recover to its original value. This is in good agreement with experimental observation. Figure 4.30 shows the comparison of the experiment profile at the inflow with the current inflow profile. It also shows the velocity profile at the injection port. As we can see, since the friction velocity goes down due to injection, higher U^+ is achieved, as expected.

Velocity vector field in the center plane for the three injection holes are shown in Fig. 4.32. In the microblowing approach, the flow from the injectors is very small and with a very small velocity. Thus, these jets interact with the viscous sublayer and the buffer layer of the incoming crossflow boundary layer. Analysis shows that the interaction is limited to a region up to $y^+ = 19$. It can be seen from this figure that whereas the jet from the leading injector penetrates further into the crossflow, the jets in its shadow have weaker impact and this shadow effect increases for the third injector.

Further analysis shows that there is a complex interaction between the various injectors. Results suggest that the wake effect of the leading injector can change the local pressure above the injectors behind it and can cause periodic reduction of the mass flow. More detailed analysis is still needed to fully understand the dynamics of

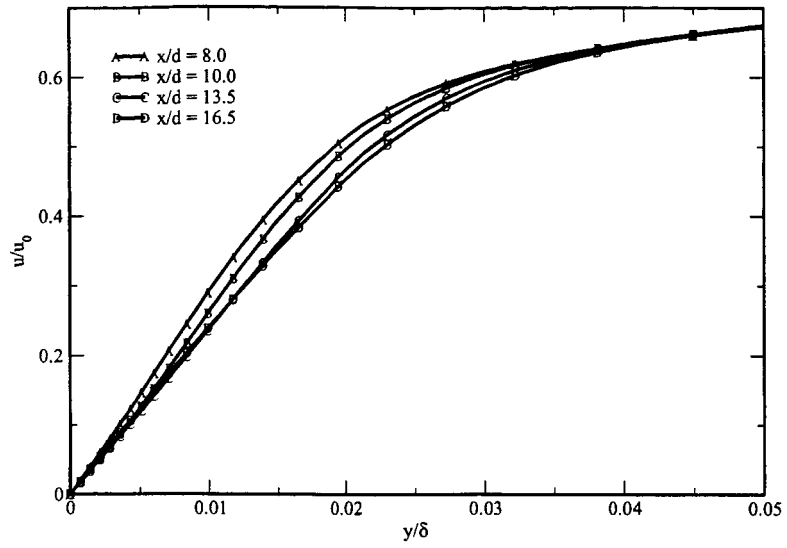

Figure 4.31: Boundary layer profile along the jet plane (y/D=0) at different x/D.

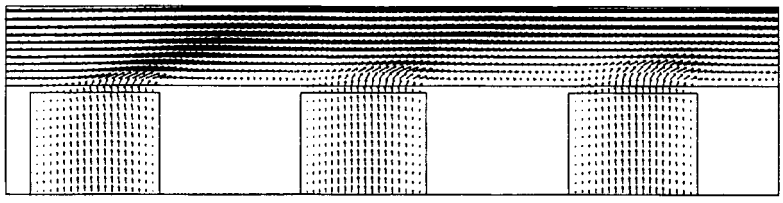

Figure 4.32: Velocity field in the center place of the three injectors. The shadow effect of the leading injector is seen on the injectors behind it.

this interaction process as a function of the injection pressure.

3D visualization of the coherent structures in the near-wall region is shown in Fig. 4.33 in the $y^+ = 4 - 19$ region. The flow is highly modulated by the presence of the micro injection and only further downstream do we see the formation of more turbulent mixed flow. Streaks in the near wall region can also be seen downstream of the martix of the holes.

Spanwise-averaged normalized coefficient of friction in stream-wise direction for two different injection ratio of 0.02 and 0.07 and shown in Fig.4.34. As observed in the experiments [4] we also observe a significant drop in skin friction drag by up to 50 percent in the immediate vicinity of the injectors.

Finally, Figs. 5.1 shows some of the flow features near the injector holes showing that there is significant interaction between the injectors. Interaction increases as the flow moves away from the plate and most of the interaction occurs in the viscous sub layer and in the buffer layer. Since most of the TKE production is in the buffer layer, this interaction results in a major modification of the near wall boundary layer profile and hence, impacts the wall shear stress and the resulting skin friction drag.

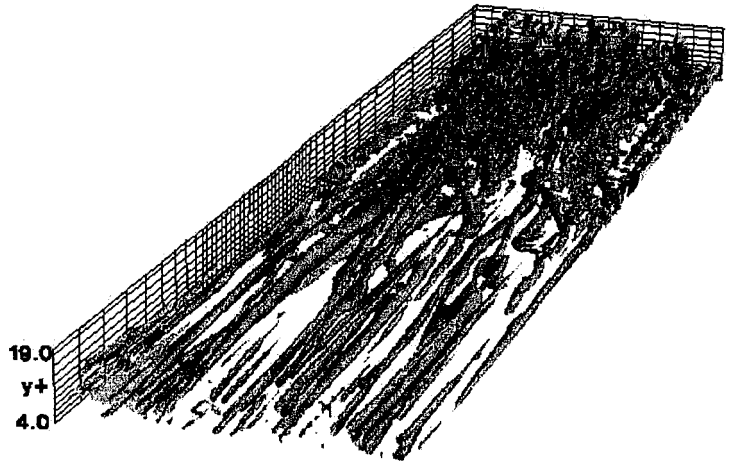

Figure 4.33: Coherent structures in the near-wall region

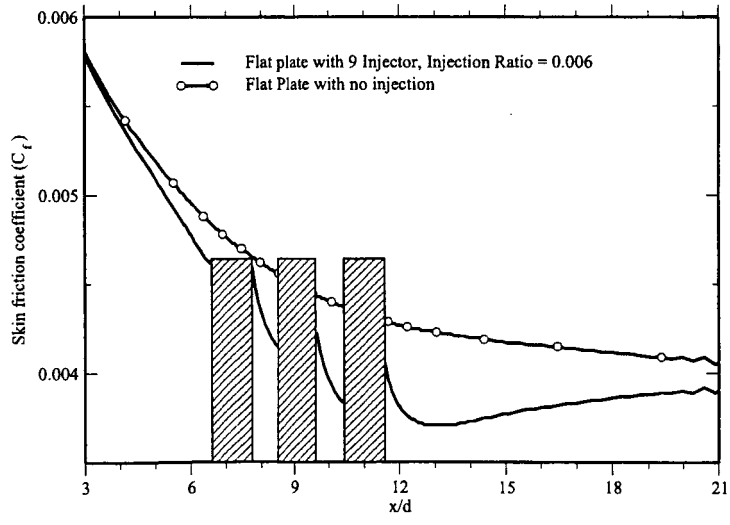

Figure 4.34: Coefficient of friction along the plate for different injection ratio.

CHAPTER V

CONCLUSIONS AND FUTURE PLANS

This final report describes the development and the evaluation of the fully coupled LBE-LES and FV-LES simulation of turbulent jet in crossflow and multiple micro-jets in crossflow. Earlier, the single free jets and jet in crossflow (JICF) were simulated using a LBE-LES method [12, 13, 10, 14, 11] and compared to experimental data. Very good agreement was obtained. Here, we simulate the same test case using the coupled formulation and compare to earlier studies to demonstrate the applicability of this coupled method. Subsequently, the coupled solver is used to simulate a matrix of 3 x 3 micro holes in a high Mach number turbulent boundary layer. This test case is similar to the experiment at NASA/GRC [4, 6] except that only a 3 x 3 matrix is simulated, whereas in the experiment, thousands of micro holes on a large flat plate were employed.

This is the first reported development of a coupled LBE-FV-LES methodology for application to micro-blowing technique. The coupled LBE-FV-LES can also be used for other possible scenarios such as film cooling injection, distributed control by fuel injection, etc.

It has been shown that this coupled approach can handle many holes simultaneously in a cost effective manner. We also believe that these sort of sub-set simulations can be used to investigate similarity features and also to develop new scaling laws. However, due to resource and time constraints, some of the planned tasks had to be truncated. Nevertheless, as this report demonstrates, we now have a hybrid LBE-FV capability to carry out LES of this complex problem.

In the current study, the LBE-LES is employed to simulate the flow inside the jet nozzles while the FV-LES is used to simulate the crossflow. A single jet in crossflow case is used for validation purpose and the results are compared with experimental data and full LBE-LES simulation. Good agreement with data is obtained. Subsequently, MBT over a flat plate with porosity of 25% is simulated using 9 jets in a compressible cross flow at a Mach number of 0.4. It is shown that MBT suppresses the near-wall vortices and reduces the skin friction by up to 50 percent. This is in good agreement with experimental data.

Currently, there are no immediate plans to further study this MBT problem since funding for this program has ended. However, it is planned to keep this code active and further improved for performance. Additional changes being considered for implementation in this code are (a) an ability to simulate circular or elliptical holes, (b) an allowance for an angled injection and (c) a more generalized subgrid closure for the LBE using the LDKM model. Some progress has already been made to achieve these objectives but more effort in validation and testing is still needed.

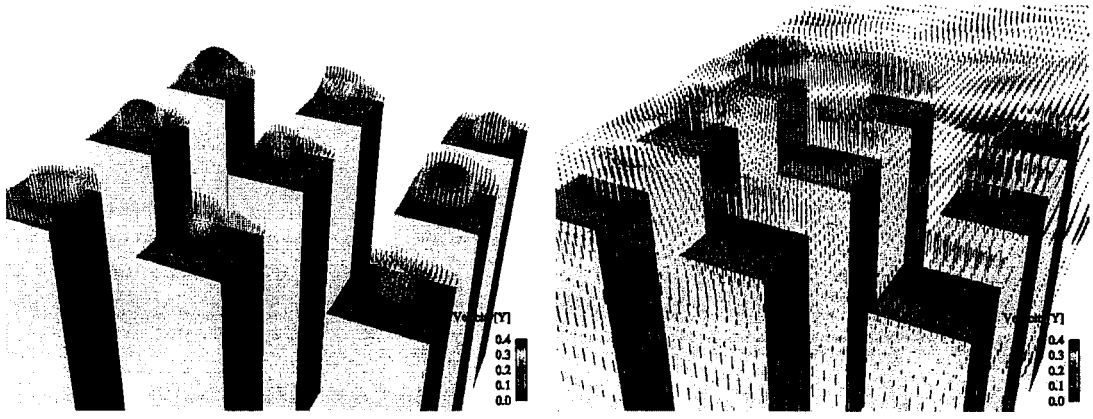

(a) y+=0

(b) y+=1.13

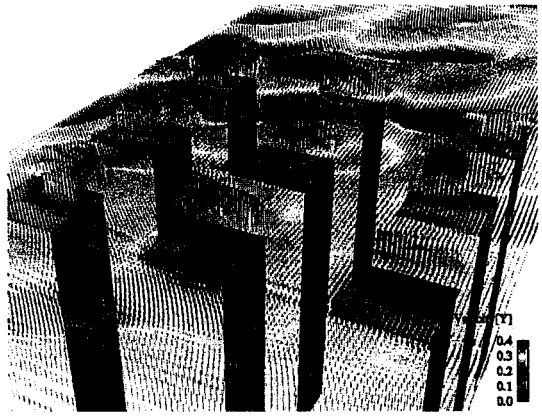

(c) y+=3.40

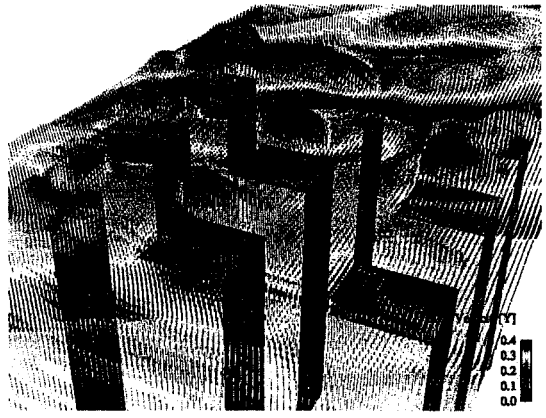

(d) y+=5.43

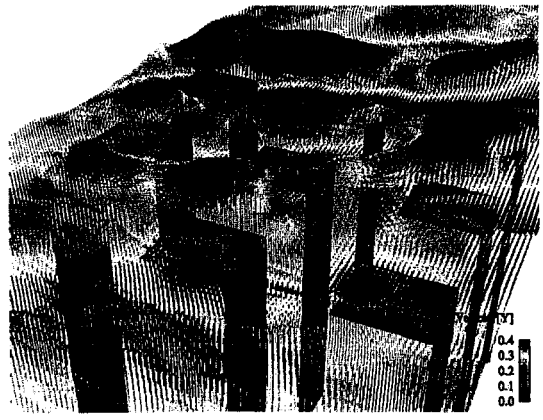

(e) y+=6.82

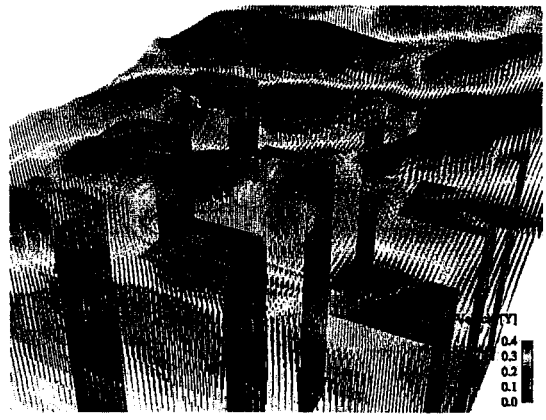

(f) y+=8.09

Figure 5.1: Normal velocity at different wall normal locations for R = 0.003

Bibliography

[1] D.P. Hwang. A proof of concept experiment for reducing skin friction by using a micro-blowing technique. *AIAA-97-0546 (NASA TM 107315)*, 1997.

[2] D. P. Hwang and T. J. Biesiadny. Experimental evaluation of the penalty associated with micro-blowing for reducing skin friction. *NASA TM 113174*, 1997.

[3] D. P. Hwang. Skin friction reduction by a microblowing technique. *AIAA J.*, 36:480–481, 1998.

[4] P. D. Hwang. Experimental study of characteristics of micro-hole porous skins for turbulent skin friction reduction. *ICAS 2002 CONGRESS*, 2002.

[5] G. E. Welch, L. M. Larosiliere, D. P. Hwang, and J. R Wood. Effectiveness of micro-blowing technique in adverse pressure gradients. *AIAA Paper No. 2001-1012*, 2001.

[6] D. P. Hwang. Review of research into the concept of the microblowing technique for turbulent skin friction reduction. *Progress in Aerospace Sciences*, 40:559–575, 2004.

[7] Y. L. Lin, M. K. Chyu, T. P. Shih, B. P. Willis, and D. P. Hwang. Skin friction reduction through micro-blowing. *AIAA Paper No. 98-0359, 36th Aerospace Sciences Meeting, Reno, NV.*, 1998.

[8] S. Menon. Computational modeling of MEMS-based micro-jets to control supersonic boundary layers. *Computational Combustion Laboratory Technical Report CCL-99-002, Georgia Tech., April 1999*, 1999.

[9] H. Wang and S. Menon. Fuel-air mixing enhancement by synthetic microjets. *AIAA Journal*, 39(12):2308–2318, 2001.

[10] S. Menon. Large-eddy/lattice boltzmann simulations of micro-blowing strategies for subsonic and supersonic drag control. *NASA Contractor Report*, CR-2003-212196, 2003.

[11] S. Menon and J.-H. Soo. Simulation of vortex dynamics in three-dimensional synthetic and free jets using the large-eddy lattice boltzmann method. *Journal of Turbulence*, 5, 2004.

[12] H. Feiz, J. H. Soo, and S. Menon. LES of turbulent jets using the lattice Boltzmann approach. *AIAA Paper 03-0780*, 2003.

[13] H. Feiz and S. Menon. LES of multiple jets in cross flow using a coupled lattice Boltzmann-finite volume solver. *AIAA Paper 03-5206*, 2003.

[14] S. Menon and H. Feiz. Blowing simulations using a coupled finite-volume lattice boltzmann les approach. *Georgia Tech Technical Report*, CCL-TR-2003-010, 2003.

[15] C. C. Nelson and S. Menon. Unsteady simulations of compressible spatial mixing layers. *AIAA-98-0786*, 1998.

[16] W.-W. Kim, S. Menon, and H. C. Mongia. Large eddy simulations of a gas turbine combustor flow. *Combustion Science and Technology*, 143:25–62, 1999.

[17] W.-W. Kim and S. Menon. Numerical modeling of turbulent premixed flames in the thin-reaction-zones regime. *Combustion Science and Technology*, 160:110–150, 2000.

[18] S. Menon. Subgrid combustion modelling for LES of single and two-phase reacting flows. In *Advances in LES of Complex Flows*, pages 329–352, 2000.

[19] G. Erlebacher, M. Y. Hussaini, C. G. Speziale, and T. A. Zang. Toward the large-eddy simulation of compressible turbulent flows. *Journal of Fluid Mechanics*, 238:155–185, 1992.

[20] U. Schumann. Subgrid scale model for finite difference simulations of turbulent flows in plane channels and annuli. *Journal of Computational Physics*, 18:376–404, 1975.

[21] S. Menon and W.-W. Kim. High reynolds number flow simulations using the localized dynamic subgrid-scale model. *AIAA Paper 96-0425*, 1996.

[22] V.K. Chakravarthy and S. Menon. Large-eddy simulations of turbulent premixed flames in the flamelet regime. *Combustion Science and Technology*, 162:175–222, 2000.

[23] V.K. Chakravarthy and S. Menon. Linear-eddy simulations of reynolds and schmidt number dependencies in turbulent scalar mixing. *Physics of Fluids*, 13:488–499, 2001.

[24] W.-W. Kim and S. Menon. A new incompressible solver for large-eddy simulations. *International Journal of Numerical Methods in Fluids*, 31:983–1017, 1999.

[25] S. Liu, C. Meneveau, and J. Katz. On the properties of similarity subgrid-scale models as deduced from measurements in a turbulent jet. *Journal of Fluid Mechanics*, 275:83–119, 1994.

[26] D. K. Lilly. A proposed modification of the germano subgrid-scale closure method. *Physics of Fluids A*, 4(3):633–635, 1992.

[27] M. Germano, U. Piomelli, P. Moin, and W.H. Cabot. A dynamic subgrid-scale eddy viscosity model. *Physics of Fluids A*, 3(11):1760–1765, 1991.

[28] U. Schumann. Realizability of reynolds-stress turbulence models. *Physics of Fluids*, 20(5):721–725, 1977.

[29] N. Patal and S. Menon. Large-eddy simulation of turbulent flow over an axisymmetric hill. *AIAA Paper 2003-0967*, 2003.

[30] C. Fureby, N. Alin, N. Wikstrom, S. Menon, N. Svanstedt, and L. Persson. On large eddy simulation of high reynolds number wall bounded flows. *AIAA Journal*, 42:457–469, 2004.

[31] C. Fureby and S.-I. Möller. Large-eddy simulation of reacting flows applied to bluff body stabilized flames. *AIAA Journal*, 33(12):2339–2347, 1995.

[32] H. Chen, S. Chen, and W.H. Matthaeus. Recovery of the Navier-Stokes equations using a lattice-gas Boltzmann method. *Physical Review A*, 45:5339–5342, 1992.

[33] Y.H. Qian, D. d'Humierès, and P. Lallemand. Lattice BGK models for the Navier-Stokes equation. *Europhysics Letters*, 17:479–484, 1992.

[34] P.L. Bhatnagar, E.P. Gross, and M. Krook. A model for collision process in gases. i. small amplitude process in charged and neutral one-component system. *Physical Review A*, 94:551–525, 1954.

[35] S. Chen and D. Doolen. Lattice Boltzmann method for fluid flows. *Annual Review of Fluid Mechanics*, 30:329–364, 1998.

[36] D. Grunau, S. Chen, and K. Eggert. A lattice Boltzmann model for multiphase fluid flows. *Physics of Fluids A*, 5:2557–2562, 1993.

[37] U. Frisch, B. Hasslacher, and Y. Pomeau. Lattice-gas automata for the Navier-Stokes equations. *Physical Review Letters*, 56:1505–1508, 1986.

[38] Y.H. Qian, S. Succi, and S.A. Orszag. Recent advances in lattice Boltzmann computing, in stauffer, d., editor. *Annual Reviews of Computational Physics III*, pages 195–242, 1995.

[39] R. Mei, W. Shyy, D. Yu, and L.S. Luo. Lattice Boltzmann method for 3d flows with curved boundary. *Journal of Computational Physics*, 161:680–699, 2000.

[40] W.-W. Kim, S. Menon, and H. Mongia. Numerical simulations of reacting flows in a gas turbine combustor. *Combustion Science and Technology*, 143:25–62, 1999.

[41] P. Lallemand and L. S. Luo. Theory of the lattice Boltzmann method: Dispersion, dissipation, isotropy, Galilean invariance, and stability. *Physical Review*, 61(6):6546–6562, 2000.

[42] D. D'Humiéres, I. Ginzburg, M. Krafczyk, P. Lallemand, and L. S. Luo. Multiple-relaxation-time lattice Boltzmann models in three dimensions. *Phil. Trans. R. Soc. Lond. A*, 360:437–451, 2002.

[43] T. J. Poinsot and S. K. Lele. Boundary conditions for direct simulation of compressible viscous flows. *Journal of Computational Physics*, 101:104–129, 1992.

[44] R. S. Maier, R. S. Bernard, and D. W. Grunau. Boundary conditions for the lattice Boltzmann method. *Physics of Fluids*, 8(7):1788–1801, 1996.

[45] C. Stone and S. Menon. Parallel simulations of swirling turbulent flames. *Journal of Supercomputing*, 22:7–28, 2002.

[46] T. F. Fric and A. Roshko. Vortical structure in the wake of the transverse jet. *Journal of Fluid Mechanics*, 279:1–47, 1994.

[47] T. T. Lim, T. H. New, and S. C. Luo. On the development of large-scale structures of a jet normal to a cross flow. *Physics of Fluids*, 13:770–775, 2001.

[48] R. M. Kelso, T. T. Lim, and A. E. Perry. An experiment study of round jets in cross-flow. *Journal of Fluid Mechanics*, 306:111–144, 1996.

[49] I. M. Milanovic and K. B. M. Q. Zaman. Highly inclined jets in cross flow. *AIAA Conference paper AIAA-2003-0183*, 2003.

[50] B. A. Haven and M. Kurosaka. Kidney and anti-kidney vortices in crossflow jets. *Journal of Fluid Mechanics*, 352:27–64, 1997.

[51] P. Ajersch, J. Zho, S. Ketler, M. Salcudean, and I. Gartshore. Multiple jets in a crossflow: detailed measurments and numerical simulations. *Journal of Turbomachinery*, 119:330–342, 1997.

[52] A. Hoda, S. Acharya, and M. Tyagi. Reynolds strees transport model predictions and large eddy simulations for film coolant jet in crossflow. *Proceedings of ASME TURBOEXPO 2000*, pages 1–15, 2000.

[53] C. K. G. Lam and K. A Bremhorst. Modified form of the k-e model for predicting wall turbulence. *Journal of Fluid Engineering*, 103:456–460, 1981.

[54] B. E. Launder and D. P. Tselepidakis. Contribution to the second-moment modeling of sub-layer turbulent transport. *Near-Wall Turbulence, Hemisphere*, pages 818–833, 1990.

[55] H. C. Chen. Submarine flows studied by second moment closure. *Journal of Engineering Mechanics*, 121:1136–1146, 1995.

[56] Lester Yuan, Robert Street, and Joel Ferziger. Large-eddy simulations of a round jet in crossflow. *Journal of Fluid Mechanics*, 379:71–104, 1999.

[57] H. Schlichting and K. Gersten. *Boundary Layer Theory.* Springer, 8th revised and enlarged edition, 2000.